Initiation phase cellular reprogramming ameliorates DNA damage in the ERCC1 mouse model of premature aging.

Patrick Treat Paine[1], Cheyenne Rechsteiner[2], Francesco Morandini[2], Gabriela Desdin Mico[1], Calida Mrabti[1], Alberto Parras[1], Amin Haghani[3], Robert Brooke[4], Steve Horvath[3,4,5], Andrei Seluanov[2], Vera Gorbunova[2], Alejandro Ocampo[1]

[1]Department of Biomedical Sciences, Faculty of Biology and Medicine, University of Lausanne, Lausanne, Vaud, Switzerland.
[2]Departments of Biology and Medicine, University of Rochester, Rochester, NY, USA
[3] Altos Labs, San Diego, USA
[4] Epigenetic Clock Development Foundation, Torrance, CA, USA
[5] Human Genetics, David Geffen School of Medicine, University of California, Los Angeles, USA

Correspondence: alejandro.ocampo@unil.ch

Keywords: progeria, DNA damage, ERCC1, accelerated aging, cellular reprogramming, TGFb

Abstract

Unlike aged somatic cells, which exhibit a decline in molecular fidelity and eventually reach a state of replicative senescence, pluripotent stem cells can indefinitely replenish themselves while retaining full homeostatic capacity. The conferment of beneficial-pluripotency related traits via in vivo partial cellular reprogramming (IVPR) significantly extends lifespan and restores aging phenotypes in mouse models. Although the phases of cellular reprogramming are well characterized, details of the rejuvenation processes are poorly defined. To understand whether epigenetic reprogramming can ameliorate DNA damage, we created reprogrammable accelerated aging mouse model with an ERCC1 mutation. Importantly, using enhanced partial reprogramming by combining small molecules with the Yamanaka factors, we observed potent reversion of DNA damage, significant upregulation of multiple DNA damage repair processes, and restoration of the epigenetic clock. In addition, we present evidence that pharmacological inhibition of ALK5 and ALK2 receptors in TGFb pathway is able to phenocopy some benefits including epigenetic clock restoration suggesting a role in the mechanism of rejuvenation by partial reprogramming.

Introduction

The phenomenon of aging is directly linked to a decline in cellular repair functions with an associated increase in aging phenotypes including genomic instability[1–3]. DNA damage events due to radiation, reactive oxygen species, chemicals, or replication errors can overwhelm DNA repair functions and are proposed as a causative factor for epigenetic dysregulation and a key contributor to age associated pathologies[4–8]. In this line, Ercc1$^{\Delta/-}$ progeroid mice, harboring a single truncated Ercc1 allele required for nucleotide excision repair (NER), interstrand crosslink repair (ICL), and homologous repair (HR) display increased DNA damage and a broad spectrum of aging phenotypes including senescence, neurodegeneration, multi-morbidity, and a shortened lifespan[9–13]. Interestingly, a recent comparative lifespan analysis of 18 wildtype rodent species indicates DNA double-strand break repair was more efficient in long-lived species[14]. For these reasons, DNA repair mutant Ercc1$^{\Delta/-}$ mice are an ideal alternative for investigating aging interventions and DNA repair-related mechanisms of rejuvenation in particular[9,15,16].

Cellular reprogramming can be defined as the conversion of a somatic cell to pluripotency and can be induced via the forced expression of four defined transcription factors; Oct4, Sox2, Klf4, and c-Myc (OSKM)[17]. The resulting induced pluripotent stem cells (iPSCs) exhibit a dedifferentiated cell identity similar to embryonic stem cells (ESCs) along with a restoration of aged phenotypes[18,19]. Recently, in vivo partial reprogramming (IVPR), following short-term cyclic expression of OSKM, has emerged as a novel therapeutic strategy for the treatment of age-related diseases (ARDs)[20–22]. Specifically, partial cellular reprogramming has produced improvements to lifespan, hallmarks of aging, the epigenetic clock, and tissue regeneration in progeroid and wildtype mouse models in vivo[6,23–34]. Multiple in vitro time course studies have demonstrated reprogramming initially

proceeds in a multifactorial manner involving extensive epigenetic remodeling, cell cycle induction with a shorted G1 phase, mesenchymal to epithelial transition due to TGFb inhibition, and BMP induction, while undergoing a major reset to the proteome and transcriptome[35–45]. Importantly, in what manner and to what extent these early alterations to molecular and cellular processes via IVPR counter and reverse aging drivers is currently unknown.

To address this limitation and gain a deeper understanding of the mechanisms involved in age amelioration by OSKM induction, we have chosen to investigate the effects of partial reprogramming in the Ercc1$^{\Delta/-}$ DNA damage model of accelerated aging. Using an in vitro time course capable of dissecting time dependent processes, we characterized the early events of reprogramming in a novel reprogrammable Ercc1$^{\Delta/-}$ accelerated aging mouse model. Most importantly, we observed a significant reduction in DNA damage beginning at 2 days of reprogramming demonstrating reversal of a key hallmark of aging. At the same time RNA seq analysis shows a significant upregulation of nearly every major DNA repair pathway while DNA methylation clock analysis shows a reversal of epigenetic age. Interestingly, improvements were more robust in the Ercc1 DNA damage model versus the wildtype cells, as would be expected from an improvement to homeostatic capacity. Lastly, small molecule inhibition of the TGFb pathway was sufficient to phenocopy some rejuvenating aspects of reprogramming including a decrease in nuclear size, decreased yH2AX, and restoration of the epigenetic clock.

Results

Induced reprogramming in a mouse model of accelerated aging decreases DNA damage

OSKM-mediated partial cellular reprogramming has been shown to mitigate genomic instability and epigenetic alterations in wildtype and Lamin A mutant mouse fibroblasts as well as in vitro aged nucleus pulposus cells[23,31]. On other hand, it is currently unknown whether this restoration would occur in an Ercc1 DNA damage model of accelerated aging with defects in DNA repair. To address this question, we developed a novel doxycycline-inducible mouse model of reprogrammable aging (Ercc1$^{\Delta/-}$ 4Fj$^{+/-}$ rtTA$^{+/-}$) containing a single truncated Ercc1 allele, Col1a1-tetO-OKSM polycistronic transgene, and the ROSA26-M2-rtTA allele (Fig. 1a).

To first verify the presence of DNA damage in our reprogrammable progeria model, adult tail tip fibroblasts (FBs) were isolated from the 4Fj Ercc1$^{\Delta/-}$ (D/KO) and 4Fj Ercc1$^{+/+}$ (WT) mice, stained for the DNA damage marker γH2AX, and imaged with confocal laser microscopy. As expected, a significant increase in yH2AX fluorescence was observed in the D/KO fibroblasts compared to the WT (Fig. 1c, s1a). In addition, this accelerated aging cell model also displayed a significant increase in nuclear area in these samples, based on nuclear staining with DAPI (Fig. S1b). This experiment confirmed the presence of a DNA repair defect in our novel OSKM inducible mouse model of aging along with an enlarged nucleus compared to WT (Fig. S1a,b).

In vitro cellular reprogramming time course experiments have previously been used to identify three phases of reprogramming including initiation, maturation, and stabilization[46,47]. Initiation phase proceeds via alterations to several key biological processes including proliferation, chromatin modification, DNA damage repair, mesenchymal to epithelial transition (MET), and RNA processing[33,41–45,48–50]. To gain insight into partial reprogramming processes with the capacity to restore homeostatic function in a DNA damage model, a time course analysis of the initiation phase of reprogramming was performed (Fig. 1b). At the same time, the induction of pluripotency in somatic cells following OSKM expression is a stochastic, asynchronous, and inefficient process often taking weeks with a low percentage of iPSC colonies[51,52]. To facilitate an accelerated reprogramming process and enhance the ability to delineate reprogramming-induced aging phenotypes in bulk cultures a previously identified small molecule combination, Vitamin C (V) and CHIR-99021 (C), was selected[53–55]. Alone, Vitamin C is able lower the epigenetic barrier of pluripotent gene expression due to its function as a histone demethylase and Tet enzyme cofactor while CHIR activates the Wnt pathway and promotes glycolysis via GSK3-beta inhibition[56–58].

To confirm the induction of cellular reprogramming following expression of OSKM in our reprogrammable DNA damage model, doxycycline (2ug/mL) was added to 4F Ercc1 cells in culture alone or combined with VC and imaged with brightfield microscopy at 4x during days 0 – 4 (Fig. 1a,b). A clear shift in cell morphology with a cobblestone appearance associated with MET is present after 2 days, more so after 4 days, and most strongly in the enhanced D4+VC group (Fig. 1e). Expression of the Klf4 and Sox2 transcription factors were observed only after doxycycline induction and most strongly at d4+VC but never day 0 based on immunofluorescence (IF) laser confocal imaging (Fig. 1d, S1c). These cells retained the fibroblast identity marker Thy1.2 at D4 with or without VC, as shown by flow cytometry, indicating this mouse model and experimental setup successfully represent initiation phase partial reprogramming without dedifferentiation or entrance into a pluripotent state (Fig. 1g, s1d).

In regards to the effects of cellular reprogramming on yH2AX in this DNA damage model, we first used flow cytometry. Specifically, two days of doxycycline induced reprogramming in the D/KO was sufficient to decrease median yH2AX fluorescent intensity per cell by 38% (Fig. S1e). Next, using IF and confocal imaging, we observed a significant decrease in mean yH2AX level per cell after 2 and 4 days of reprogramming (Fig. 1g, h, S1j). Similarly, enhanced reprogramming with VC also restored this DNA damage marker significantly after 2 and 4 days of OSKM induction (Fig. 1g, h, S1j). These D/KO cells also displayed a significant reduction in nuclear size during reprogramming after induction with doxycycline for 2 or 4 days (Fig. 1i). When this experiment was repeated on OSKM inducible WT cells without the DNA repair defect, it also showed a significant decrease in yH2AX signal and decrease in nuclear area (Fig. S1f). Thus, initiation phase cellular

reprogramming is sufficient to ameliorate a key driver of aging even in mutant cells defective for DNA repair responsible for NER, ICL, and HR.

The DNA methylation clock is restored in Ercc1$^{\Delta/-}$ following short term reprogramming

Recent evidence from our lab indicates that D/KO FBs display accelerated aging based on the DNA methylation clock and are therefore a good *in vitro* model to investigate aging mechanisms and interventions[59]. Furthermore, cellular reprogramming has been observed to reverse epigenetic age in mouse and human cell types but the effects on an accelerated aging model with a DNA repair defect are unknown[60,61]. In order to investigate the effect of reprogramming on the DNA methylation clock, we applied the DNA Methyl Age Skin Final clock to all samples and timepoints. Strikingly, enhanced reprogramming with VC for 4 days in the D/KO produced a significant restoration to the DNA methylation clock with the top responder showing a 54% decrease in epigenetic age (Fig. 2a). At the same time, there was a trend towards epigenetic clock restoration after 2 and 4 days of reprogramming although not significant, perhaps due to less efficient reprogramming (Fig. 2a). Significant restoration to the DNAm clock only occurred at day 2 in WT FBs (Fig. s2a). In addition, variability was greater in the WT samples perhaps due to the stochastic nature of reprogramming and the early time point chosen for analysis, or the lack of accelerate aging phenotype (Fig. s2a). The robust reversal of the DNAm clock in the D/KO FBs indicates enhanced reprogramming is capable of cellular rejuvenation in an aging model with defective DNA repair.

Next, as chromatin remodeling and reversal of the DNA methylation clock are observed to coincide during cellular reprogramming, we sought to understand the epigenetic alterations that occur following reprogramming in this Ercc1 model[48,61]. First, a significant increase in H3K9me3 was observed in the D/KO fibroblasts compared to WT controls based on IF confocal imaging at 100x (Fig. 2b, s2b). A similar increase was observed in the heterochromatin mark H4K20me3 while H3K27me3 remained unchanged under the same conditions (Fig. s2d, e). These results were then confirmed with western capillary analysis (Fig s2c). We hypothesize that this *in vitro* phenotype of chromatin compaction is an adaptation in these cells to protect against chronic elevated DNA damage levels[62,63]. Interestingly, when reprogramming or enhanced reprogramming was induced for 2 or 4 days, heterochromatin was significantly decreased in this DNA damage model shifting it towards wildtype levels (Fig. 2c, d, e, s2g, h, I, and j). This restoration of heterochromatin levels in D/KO FBs coincides with improvement to reversion of the DNAm clock, in line with previous reports suggesting a mechanistic relationship[6,23,32].

Homeostatic capacity is significantly upregulated during the initiation phase of cellular reprogramming

To better understand the effects of reprogramming in this DNA damage model, paired-end bulk RNA sequencing and analysis was performed for each treatment and time point. Principal component analysis (PCA) based on relative gene expression values confirmed groups clustered based on the treatment, timepoint, and cell type while displaying a reprogramming trajectory from day 0 to day 4 (Fig. 3a). Interestingly, the enhanced reprogramming at day 2 plus VC was equal to 4 days of reprogramming alone based on overlapping PCA scores (Fig. 3a). At the same time, D/KO cells displayed a larger shift in PC2 score than WT following reprogramming (Fig. 3a). Venn diagrams and associated gene expression heat maps were created based on the normalized transcriptomes from each group and demonstrate a shared gene profile during reprogramming albeit with some unique differences (Fig. 3b, 3c). In particular, over 1400 genes were uniquely upregulated and 992 downregulated in the D/KO Fbs during initiation phase with enhanced reprogramming compared to reprogrammed WT cells (Fig. 3c). The most robust changes were observed following enhanced reprogramming to the D/KO group, indicating a profound and rapid reset to the transcriptome in this DNA damage model (Fig. 3b, 3c). GO term analysis demonstrated a significant upregulation of DNA damage repair pathways in the D/KO enhanced reprogramming group including DNA repair, homologous recombination (HR), non-homologous end joining (NHEJ), base excision repair (BER), mismatch repair (MMR), nucleotide excision repair (NER), and alternative end joining (AltEJ), while interstrand crosslink repair (ICR) showed a trend towards upregulation. (Fig. 3d, S3a). At the same time, reprogramming in WT cells did not produce such broad and robust effects on DNA repair processes (Fig. 3d, S3a). Other notable processes increased with enhanced reprogramming include chromatin organization pathways in D/KO cells (Fig. 3d, S3a). Importantly, there was also a significant downregulation in TGFb receptor signaling and TGFb regulation pathways as well as a decrease in EMT pathways (Fig. 3d, S3a). Gene set enrichment analysis (GSEA) showed that intermediate filament cytoskeleton organization and processes, keratinocyte differentiation and epidermal differentiation were significantly upregulated at all timepoints and models (Fig. S3b). At the same time, Reactome analysis showed that Keratinization and Formation of the Cornified Envelope were also universally upregulated (Fig. S3c). Together, this transcriptomic data provides a mechanistic basis that supports the observed changes to morphological, epigenetic, and DNA damage phenotypes that occur following short-term reprogramming in our DNA damage model. Interestingly, the robust upregulation of major DNA repair processes in the Ercc1 model vs WT suggest a homeostatic process capable of responding to intrinsic molecular and age-related defects that characterized Ercc1 cells.

TGFb inhibition alone improves DNA damage phenotypes and rejuvenates the DNA methylation clock

The RNA seq analysis showing downregulation of TGFb signaling and associated epithelial to mesenschymal transition pathways is a well-documented early event of cellular reprogramming following OSKM induction[35,40,41,64]. In contrast, upregulation of TGFb signaling is a driver of aging

phenotypes including cell degeneration, fibrosis, ROS, inflammation, DNA damage, senescence, and stem cell aging[65–68]. Recently our lab observed that inhibition of the TGFb pathway is able to extend lifespan in C. elegans, supporting its role in aging and longevity[69]. Based on these observations, we asked whether TGFb inhibition alone could impact DNA damage and the DNA methylation clock in our Ercc1 accelerated aging model in a manner similar to reprogramming (Fig. 3a). In this line, the TGFb superfamily consists of over 30 subtypes but for this study we focused on canonical TGFb signaling and the bone morphogenic protein pathway (BMP) as both have been identified to be important for early stage reprogramming [41,53,70]. Specifically, 9 inhibitors that target the TGFb ALK5 receptor and 6 inhibitors that target the BMP ALK2 receptors were screened for 3 days on D/KO fibroblasts. Following a cell viability study to confirm a safe dosage range, a high or low dose of each inhibitor was added to the Ercc1 fibroblasts for 3 days and analyzed for changes to yH2AX using IF and confocal microscopy (Fig. S4a). Surprisingly, all of the ALK5 inhibitors successfully decreased yH2AX levels based on IF, although in some cases it was dose-dependent (Fig. 4b). Similarly, all but one of the ALK2 inhibitors also decreased DNA damage in Ercc1 fibroblasts, although not as effectively as the ALK5 inhibitors, again in a dose dependent manner (Fig. 4c). Subsequently, we repeated these experiments with only the top performers including ALK5 inhibitors Repsox and A83-01, ALK2 inhibitor DMH-1, and dual ALK5 and ALK2 inhibitor Vactosertib. Once again, each of the inhibitors decreased the yH2AX signal of Ercc1 fibroblasts below control levels although the ALK2 inhibitor, DMH-1, was less effective than the three ALK5 inhibitors (Fig. s4b). Interestingly, when nuclear area was calculated based on DAPI staining, DMH-1 was also the only inhibitor not to show a trend towards decreased nuclear size potentially implying an association between nuclear size changes and improvements in DNA repair (Fig. s4). In contrast, other small molecules previously shown to induce pluripotency when applied as a cocktail were unable to decrease yH2AX levels in Ercc1 fibroblasts when applied individually including valproic acid (VPA), CHIR, tranylcypromine (TCP), Forskolin, DZNep, or TTNPB (Fig. s4c) [71,72]. When the ALK5 inhibitor, Repsox, was combined with 4 days of reprogramming, no added benefit to yH2AX levels was observed (Fig. S4d). Finally, significant rejuvenation of the DNA methylation clock was observed with 3 of the 4 inhibitors, including Repsox, A83-01, and DMH-1 (Fig. 4d). This data demonstrates that ALK5 and ALK2 inhibition is able reduce DNA damage and restore the DNA methylation clock in this Ercc1 accelerated aging model.

RNA-seq analysis was next performed in Ercc1 FBs following treatment with these four TGFb inhibitors to better understand the mechanistic basis for improved DNA damage and a rejuvenated DNA methylation clock with ALK2 or ALK5 inhibition. Notably, PCA scores show the three ALK5 inhibitors cluster tightly together compared to the ALK2 inhibitor (Fig. 4e). Interestingly, all 4 inhibitors shifted the D/KO transcriptome along the PC2 axis in the direction of WT cells with the greatest change observed following treatment with A83-01 (Fig. 4e). At the same time, Venn diagrams show 558 genes were upregulated and 371 downregulated by all 4 inhibitors indicating similarity in gene expression profile regardless of target receptor (Fig. 4f). Next, gene set

enrichment analysis (GSEA) shows significant decreases to spindle checkpoint signaling with Repsox, Vactosertib, and A83-01 but not with DMH-1 (Fig. S4e). DMH-1 had a unique effect on upregulation of response to virus, response to interferon-gamma, and response to interferon-beta among others based on the GSEA (Fig. S4e). Repsox uniquely induced upregulation to developmental-related gene sets including embryonic hindlimb morphogenesis, hindlimb morphogenesis, and midbrain development (Fig. S4e). Reactome analysis showed that DMH-1 also uniquely increased interferon signalling (Fig. S4e). Interestingly, GO term analysis demonstrated that all four inhibitors significantly downregulated several biological processes including mitotic cell cycle and canonical glycolysis (Fig. S5a). In line with previous publications showing TGFb inhibition disrupts DNA repair processes in cancer cells and HSCs, these four inhibitors also disrupted several DNA repair proceses in our Ercc1 FBs (Fig. S5a)[65,73–75]. Interesting exceptions include a significant improvement to NER by DMH-1 and a trend towards upregulated ICL repair amongst all (Fig. S5a) Together this data shows ALK5 and ALK2 inhibitors are capable of decreasing the DNA damage marker yH2AX and restoring the DNA methylation clock in Ercc1 fibroblasts while sharing some changes to the transcriptomic profiles.

TGFb inhibition phenocopies aspects of initiations phase cellular reprogramming

To investigate and compare shared rejuvenation processes between cellular reprogramming and TGFb inhibition, we next evaluated significant transcriptomic changes among the different treatments. Notably, a heatmap of significantly up or down regulated genes among the different treatments indicate a similar profile (Fig. 5c). Specifically, 684 shared DEGs were upregulated and 627 downregulated following treatment with the ALK5 inhibitors Repsox, A83-01, Vactosertib, and reprogramming at day 4 (Fig. 5a). Notably, gene expression changes induced by the 4 inhibitors shared a positive correlation with gene expression changes induced by reprogramming (Fig. 5b). The strongest correlation was observed between the three ALK5 inhibitors and D4 reprogramming (Fig. 5b, S5b). Interestingly, A83-01 was the closest in transcriptomic profile to day 4 reprogramming while Repsox was the closest to D4 enhanced reprogramming (Fig. 5b, S5b). The top GO terms that were significantly downregulated with either reprogramming or the TGFb inhibitors include external encapsulating structure organization, extracellular matrix organization, extracellular structure organization, collagen fibril organization, skeletal system development and protein hydroxylation (Fig. 5d). The most significantly upregulated GO terms shared by both D4 reprogramming and TGFb inhibition include steroid biosynthetic process, regulation. of steroid biosynthetic process, alcohol biosynthetic process, organic hydroxyl compound metabolic process, epidermal cell differentiation, and alcohol metabolic process (Fig. 5d). Reactome analysis of shared processes between reprogramming and Repsox, A83-01, and Vactosertib showed upregulation of complement cascade and downregulation of collagen formation and ECM organization (Fig. 5e).

Interestingly, significant differences were noted when comparing the transcriptomic effects of reprogramming vs TGFb inhibition on DNA repair processes even though both improved the DNA damage phenotype. Specifically, TGFb inhibition significantly downregulated multiple DNA repair processes in Ercc1 fibroblasts including AltEJ, NHEJ, and HR among others while reprogramming significantly upregulated them (Fig. S5a 3b). At the same time, only DMH-1 matched reprogramming by significantly upregulating NER, while Repsox and Vactosertib showed a trend towards improvment (Fig. s5a). In sum, this transcriptomic data demonstrates that TGFb inhibition and initiation phase reprogramming share a strong correlation in changes to gene expression. At the same time, reprogramming induces a more robust effect, especially on DNA repair processes in our reprogrammable Ercc1 aging model.

Discussion

Although the age ameliorating effects of in vivo partial reprogramming have been well documented, the mechanistic drivers of rejuvenation by reprogramming are currently lacking[18]. Interestingly, the robust alterations to biological processes that occurs during the initiation phase of cellular reprogramming including proliferation, chromatin modification, DNA damage repair, MET, and RNA processing are well characterized and could potentially represent mechanistic drivers of longevity[41–45,48]. For these reasons, we investigated the relationship between these early reprogramming induced changes and their impact on aging phenotypes. Specifically, we developed a reprogrammable DNA damage model of accelerated aging, Ercc1$^{\Delta/-}$ 4Fj$^{+/-}$ rtTA$^{+/-}$, in order to test the impact of initiation phase reprogramming on a key driver of aging, genomic instability. As OSKM inhibits TGFb signaling and drives the MET during initiation phase reprogramming, we investigated the mechanistic basis of rejuvenation via cellular reprogramming by comparing it to TGFb inhibition[46]. Due to the slow, stochastic, and asynchronous reprogramming process which confounds molecular studies in bulk cultures we also utilized a previously defined enhanced method of cellular reprogramming by adding ascorbic acid and CHIR-99021 to the culture media[53,56,57].

Here we observed that OSKM expressing Ercc1 cells undergo robust reprogramming induced changes to morphology, nuclear size, epigenome, transcriptome, and homeostasis related DNA repair processes. Striking improvements to the DNA damage marker yH2AX in our Ercc1 fibroblasts with a defective repair process occurred within 2 days of pluripotency factor expression. At the same time, the elevated heterochromatin markers H3K9me3 and H4K20me3 were significantly restored following enhanced reprogramming for 2 and 4 days. Most notably, DNA methylation clock analysis shows significant rejuvenation in these Ercc1 cells after 4 days of enhanced reprogramming. RNA sequencing analysis of the transcriptome showed several GO processes were upregulated significantly including DNA repair, chromatin organization, and mitotic cell cycle. This is consistent with pluripotency transcription factors being upstream of DNA repair

processes, particularly DNA double-strand break repair that repairs damage marked by yH2AX[76]. Simultaneously, TGFb signaling and EMT processes were significantly downregulated.

As TGFb signaling is a driver of many aging phenotypes, we further investigated the importance of this signaling pathway to reprogramming induced rejuvenation via inhibition of the TGFb receptor ALK5 or the BMP receptor ALK 2[67,70]. Interestingly, nearly every TGFb inhibitor tested significantly decreased yH2AX levels in Ercc1 fibroblasts. The ALK5 inhibitors showed a more robust impact than ALK2 inhibitors on yH2AX levels while also decreasing nuclear size, a common phenotype observed during reprogramming. Importantly, rejuvenation of the epigenetic clock was observed following treatment with 3 of 4 TGFb inhibitors in this accelerated aging model. At the same time, RNA analysis showed a strong correlation between TGFb inhibition and reprogramming based on similar changes to hundreds of DEGs. Interestingly, the robust changes to DNA repair based on GO pathway analysis was unique to OSKM expression. Previous work has shown that activation of the TFGb pathway promotes genomic instability and induces HR defects while inhibition reduces DNA damage, senescence, and aging phenotypes[67,74,77,78]. Interestingly, TGFb inhibition has a disruptive effect on many DNA repair processes while selectively promoting others in a cell type specific manner similar to our observations[65,75].

Although initiation phase reprogramming in wildtype and Ercc1 fibroblasts was capable of ameliorating the DNA damage marker yH2AX, the scale of effect was far more robust in the DNA damage model as demonstrated by significant increases in all major DNA repair processes. This data suggests that cellular reprogramming is sensitive to intrinsic cell state cues and drives a restoration of homeostatic function and youthful molecular phenotypes. Similarly, in vivo partial reprogramming studies show a more robust improvement to lifespan in progeria models indicating an ability to respond to deleterious cell states[23,25] Previously, it was shown improved DNA repair via overexpression of the HR protein Rad51 enhances reprogramming efficiency[79]. In our 4F Ercc1 fibroblasts, we observed the most significant reprogramming-induced rejuvenation coincided with upregulation of multiple DNA repair pathways. Recently maturation phase transient reprogramming for 13 days was shown to reverse the epigenetic clock in aged donors by up to 30 years but longer periods saw diminished benefits[33]. Other groups have shown a single short burst of reprogramming in vivo is sufficient to ameliorate aging hallmarks and tissue-specific physiology[25]. The precise mechanism of rejuvenation involved is unknown although several studies, including ours, supports a mechanistic contribution from the epigenetic remodeling process[6,7,32,80]. Importantly, by inducing initiation phase reprogramming in an Ercc1 model with an accelerated epigenetic clock, we observed early reprogramming coincided with TGFb inhibition, improved homeostasis, DNA repair, and epigenetic rejuvenation. Notably, attempts to replicate OSKM-induced TGFb inhibition with small molecule inhibitors phenocopied improvements to the epigenetic clock in this Ercc1 model while decreasing the DNA damage marker yH2AX.

Transcriptomic comparisons between cellular reprogramming and TGFb inhibitors of the ALK5 and ALK2 receptors were positively correlated and shared similar changes to hundreds of DEGs. At the same time, the robust upregulation of DNA repair processes via initiation phase reprogramming compared to TGFb inhibition alone suggests a different mechanistic route to DNA damage repair.

In conclusion, delineating the specific basis of rejuvenation remains difficult and potentially confounded by the multifactorial sequence of events necessary for reprogramming to proceed . The data here supports the premise that TGFb inhibition is a mechanistic contributor to rejuvenation induced by cellular reprogramming. This work sets the stage for further mechanistic investigations into the early events of reprogramming to better understand the associated drivers of rejuvenated phenotypes.

Conflict of interest

S.H. is the founder of the non-profit Epigenetic Clock Development Foundation that licenses patents from his former employer UC Regents, and he is listed as the inventor. The remaining authors declare no conflicts of interest.

Author contributions

A.O. and P.T.P. designed the study. A.O., A.H., R.B., S.H. and P.T.P. were involved in all experiments, data collection, analysis and interpretation. A.P and P.T.P generated the mice strains. P.T.P. and C.R. prepared the figures. C.M. performed skin fibroblast extractions. C.R., F.M., A.S., V.G. and P.T.P. prepared and analyzed RNA-seq data. A.O., P.T.P., and G.M. provided guidance. P.T.P wrote the manuscript with input from authors.

Data availability statement

The data can be made available from the corresponding author upon request.
The mammalian methylation array is from the nonprofit Epigenetic Clock Development Foundation (https://clockfoundation.org/).

Code availability statement

The RNA-seq analysis code is available at https://github.com/cheyennerechsteiner/Ercc1-Reprogramming.

Methods

Animal housing

These experiments were performed in accordance with Swiss legislation and after approval from the local authorities (Cantonal veterinary office, Canton de Vaud, Switzerland). Mice were housed in groups of five per cage or less with a 12hr light/dark cycle between 06:00 and 18:00 in a

418 temperature-controlled environment at 25°C and humidity between 40 % and 70 %, with access to
419 water and food. Wild type, premature aging, and programmable mouse models generated were
420 housed together in the Animal Facilities of Epalinges and Department of Biomedical Science of
421 the University of Lausanne.
422
423 **Mouse strains**
424 Ercc1$^{\Delta/-}$ mice and littermate controls Ercc1$^{+/+}$ were generated in a C57BL6J|FVB hybrid
425 background as previously generated and described by de Waard [13]. Reprogrammable 4Fj$^{+/-}$ rtTA$^{+/-}$
426 Ercc1$^{\Delta/-}$ (4F.D/KO) and 4Fj$^{+/-}$ rtTA$^{+/-}$ Ercc1$^{+/+}$ (4F.WT) mice strains were generated in a
427 C57BL6J|FVB hybrid background following crosses with the previously described 4Fj mouse
428 developed by Rudolf Jaenisch [82]. Previously described wildtype reprogrammable cells with an
429 Oct4-EGFP reporter were derived from mice carrying a polycistronic cassette containing Oct4,
430 Sox2, Klf4, c-Myc, and a single allele EGFP in the Col1a1 locus (OKSM)[83].
431
432 **Mouse monitoring and euthanasia**
433 All mice were monitored three times per week for their activity, posture, alertness, body weight,
434 presence of tumors or wound, and surface temperature. Males and females were euthanized at by
435 CO_2 inhalation (6 min, flow rate 20% volume/min). Subsequently, tail tip fibroblasts were harvested
436 and cultured.
437
438 **Cell culture and maintenance**
439 Tail tip fibroblasts (TTF) were extracted from mice using Collagenase I (Sigma, C0130) and
440 Dispase II (Sigma, D4693) and cultured in DMEM (Gibco, 11960085) containing 1% non-essential
441 amino acids (Gibco, 11140035), 1% GlutaMax (Gibco, 35050061), 1% Sodium Pyruvate (Gibco,
442 11360039) and 10% fetal bovine serum (FBS, Hyclone, SH30088.03) at 37°C in hypoxic conditions
443 (3% O2). Subsequently, fibroblasts were cultured and passaged (3 or less) according to standard
444 protocols. Reprogrammable TTF cells used in experiments were from young mice, including 4Fj$^{+/-}$
445 rtTA$^{+/-}$ Ercc1$^{\Delta/-}$ and 4Fj$^{+/-}$ rtTA$^{+/-}$ Ercc1$^{+/+}$ (8 week old male), and 4FJ$^{+/-}$ OCT4-GFP TTF (22 week
446 old female). Non-reprogramming Ercc1 TTF used include Ercc1$^{\Delta/-}$ and Ercc1$^{+/+}$ (8 week old male)
447 Experiments for TGFb inhibitors used Ercc1$^{\Delta/-}$ cells (4 week old female) and Ercc1$^{+/+}$ TTF cells (14
448 week old female). Induction of the OSKM reprogramming factors in vitro followed treatment with
449 doxycycline 2ug/ml in culture media for the specified time points. Enhanced reprogramming
450 followed the same protocols but added fresh ascorbic acid (50ug/ml) and CHIR-99201 (3uM) as
451 previously reported[53].
452
453 **Immunofluorescence staining**
454 Following experiments in 96 well plates or 24 well plates, TTF were washed with fresh PBS and
455 fixed with 4% paraformaldehyde (Roth, 0964.1) in PBS at room temperature (RT) for 15 minutes.

Then cells were washed 3 more times, followed by blocking and permeabilization step in 1% bovine serum albumin (Sigma, A9647-50G) in PBST (0.2% Triton X-100 in PBS) for 1 hour (Roth, 3051.3). TTF were then incubated at 4°C overnight with a primary antibody, washed in PBS, followed by incubation with a secondary antibody and DAPI staining at room temp. for 1 hour. If performed in 24 well plates, coverslips were used and mounted with Fluoromount-G (Thermofisher, 00-4958-02), dried at RT in the dark, and stored at 4°C until ready to image or -20°C for long-term.

Immunofluorescence imaging

Confocal image acquisition was performed using the NIKON Ti2 Yokogawa CSU-W1 Spinning Disk, using the 100X objective and with 15 z-sections of 0.3 µm intervals. Lasers for each antibody were selected (405 nm and 488 nm) with a typical laser intensity set. Exposure time and binning were established separately to assure avoidance of signal saturation.

Antibodies and compounds

Antibodies include: Abcam: anti-H3K27me3 (ab192985); Cell Signaling: anti-H3K9me3 (13969), anti-H4K20me3, anti-γH2AX (9718); Roth: DAPI (6843.1) Compounds include: Cayman; Valproic Acid (13033), CHIR99021 (13122), Repsox (14794), Forskolin (11018), Doxorubicin (15007); Acros Organics: TCP (130472500); APExBIO: DZNep (A8182); Seleckchem: TTNPB (S4627); Roth: X-beta-Gal (2315.3), Ascorbic Acid (Sigma).

Flow cytometry

Cells were stained with Thy1.2-APC and SSEA1-PE (Biolegend). Cells were fixed in BD Fixation and Permeabilization Solution. A Bechman Coulter Cytoflex S flow cytometer determined cellular subpopulation ratios.

RNA sequencing, processing, analysis

Total RNA and DNA was extracted from the same samples. Total RNA was extracted from cells using the Qiagen AllPrep DNA/RNA Micro Kit (New England Biolab) and protocols were followed. Total RNA concentrations were determined using the Qubit RNA BR Assay Kit (Thermofisher, Q10211).

The RNA-Seq library preparation and sequencing was done by Novogene (UK) Company Limited on an Illumina NovaSeq 6000 in 150 bp paired-end mode. Raw FASTQ files were evaluated for quality, adapter content and duplication rates with FastQC. Reads were trimmed using TrimGalore! (https://www.bioinformatics.babraham.ac.uk/projects/trim_galore/) and aligned to the GRCm39 mouse genome assembly using Hisat2 (https://doi.org/10.1038/s41587-019-0201-4). Number of reads per gene were measured using the featureCounts function in the subread package[84].

All subsequent analysis was performed in R. DESeq2 was used to normalize raw read counts and perform differential gene expression analysis (doi:10.1186/s13059-014-0550-8). Ensembl gene IDs were mapped to gene symbols via the mapIds function in the AnnotationDbi package (Pagès H, Carlson M, Falcon S, Li N (2023). *AnnotationDbi: Manipulation of SQLite-based annotations in Bioconductor*) with an org.Mm.eg.db reference package (Carlson M (2019). *org.Mm.eg.db: Genome wide annotation for Mouse*). The clusterProfiler package (doi:10.1089/omi.2011.0118, doi:10.1016/j.xinn.2021.100141) was used to perform gene set enrichment analysis (GSEA) on gene ontology and Reactome terms.

DNA extractions

Total DNA was extracted from cells using the Qiagen AllPrep DNA/RNA Micro Kit (New England Biolab) and protocols were followed. Total DNA concentrations were determined with the Qubit DNA BR Assay (Thermofisher, Q10211).

DNA methylation clock

Methylation data was generated via the HorvathMammalMethylChip[85] and normalized with the SeSaMe method[86]. Human methylation data were generated on the Illumina EPIC array platforms which profiles 866k cytosines. The noob normalization method was used and implemented in the R function preprocess Noob. The DNAm age was estimated using the DNAm Age Skin Final clock algorithm.[87]

MTS cell proliferation assay

Cell viability was performed with Tetrazolium MTS assay. Cells were cultured for 1 day in 96-well plates and treated with small molecules for 3 consecutive days prior to incubation with 120 µL fresh media containing 20 µL of CellTiter 96® AQueous One Solution (Promega, G3580) for 1 to 4 hours at 37°C in a humidified, 5% CO2 atmosphere. The absorbance was determined at 490nm using a BioTek Epoch 2 microplate reader. The proportion of viable cells was determined as a ratio between the observed optical density (OD) compared to control OD.

Quantification and statistical analysis

Analysis of immunofluorescence microscopy images was performed using FIJI. Typically, 20 different ROIs were imaged at 100x from each well from three experiments unless otherwise noted. Maximal projections of z-stacks were analyzed and total fluorescence intensity per cell and total nuclear area were determined.

All statistical analysis, statistical significance and n values are reported in the figure legends. Statistical analyses were performed using GraphPad Prism 9.0.0.

References

1. Rando, T. A. & Chang, H. Y. Aging, Rejuvenation, and Epigenetic Reprogramming: Resetting the Aging Clock. *Cell* **148**, 46–57 (2012).
2. Kennedy, B. K. *et al.* Geroscience: Linking Aging to Chronic Disease. *Cell* **159**, 709–713 (2014).
3. López-Otín, C., Blasco, M. A., Partridge, L., Serrano, M. & Kroemer, G. The Hallmarks of Aging. *Cell* **153**, 1194–1217 (2013).
4. Schumacher, B., Pothof, J., Vijg, J. & Hoeijmakers, J. H. J. The central role of DNA damage in the ageing process. *Nature* **592**, 695–703 (2021).
5. Niedernhofer, L. J. *et al.* Nuclear Genomic Instability and Aging. *Annu. Rev. Biochem.* **87**, 295–322 (2018).
6. Yang, J.-H. *et al.* Loss of epigenetic information as a cause of mammalian aging. *Cell* **186**, 305-326.e27 (2023).
7. Kane, A. E. & Sinclair, D. A. Epigenetic changes during aging and their reprogramming potential. *Crit. Rev. Biochem. Mol. Biol.* **54**, 61–83 (2019).
8. Tubbs, A. & Nussenzweig, A. Endogenous DNA Damage as a Source of Genomic Instability in Cancer. *Cell* **168**, 644–656 (2017).
9. Vermeij, W. P. *et al.* Restricted diet delays accelerated ageing and genomic stress in DNA-repair-deficient mice. *Nature* **537**, 427–431 (2016).
10. Li, W. *et al.* Nucleotide excision repair capacity increases during differentiation of human embryonic carcinoma cells into neurons and muscle cells. *J. Biol. Chem.* **294**, 5914–5922 (2019).
11. Weeda, G. *et al.* Disruption of mouse ERCC1 results in a novel repair syndrome with growth failure, nuclear abnormalities and senescence. *Curr. Biol.* **7**, 427–439 (1997).
12. Dollé, M. E. T. *et al.* Increased genomic instability is not a prerequisite for shortened lifespan in DNA repair deficient mice. *Mutat. Res. Mol. Mech. Mutagen.* **596**, 22–35 (2006).
13. de Waard, M. C. *et al.* Age-related motor neuron degeneration in DNA repair-deficient Ercc1 mice. *Acta Neuropathol. (Berl.)* **120**, 461–475 (2010).

14. Tian, X. *et al.* SIRT6 Is Responsible for More Efficient DNA Double-Strand Break Repair in Long-Lived Species. *Cell* **177**, 622-638.e22 (2019).
15. Takayama, K. *et al.* mTOR signaling plays a critical role in the defects observed in muscle-derived stem/progenitor cells isolated from a murine model of accelerated aging. *J. Orthop. Res.* **35**, 1375–1382 (2017).
16. Birkisdóttir, M. B. *et al.* Unlike dietary restriction, rapamycin fails to extend lifespan and reduce transcription stress in progeroid DNA repair-deficient mice. *Aging Cell* **20**, e13302 (2021).
17. Takahashi, K. & Yamanaka, S. Induction of Pluripotent Stem Cells from Mouse Embryonic and Adult Fibroblast Cultures by Defined Factors. *Cell* **126**, 663–676 (2006).
18. Singh, P. B. & Newman, A. G. Age reprogramming and epigenetic rejuvenation. *Epigenetics Chromatin* **11**, 73 (2018).
19. Lapasset, L. *et al.* Rejuvenating senescent and centenarian human cells by reprogramming through the pluripotent state. *Genes Dev.* **25**, 2248–2253 (2011).
20. Mahmoudi, S., Xu, L. & Brunet, A. Turning back time with emerging rejuvenation strategies. *Nat. Cell Biol.* **21**, 32–43 (2019).
21. de Magalhães, J. P. & Ocampo, A. Cellular reprogramming and the rise of rejuvenation biotech. *Trends Biotechnol.* **40**, 639–642 (2022).
22. Alle, Q., Le Borgne, E., Milhavet, O. & Lemaitre, J.-M. Reprogramming: Emerging Strategies to Rejuvenate Aging Cells and Tissues. *Int. J. Mol. Sci.* **22**, 3990 (2021).
23. Ocampo, A. *et al.* In Vivo Amelioration of Age-Associated Hallmarks by Partial Reprogramming. *Cell* **167**, 1719-1733.e12 (2016).
24. Macip, C. C. *et al.* Gene Therapy Mediated Partial Reprogramming Extends Lifespan and Reverses Age-Related Changes in Aged Mice. 2023.01.04.522507 Preprint at https://doi.org/10.1101/2023.01.04.522507 (2023).
25. Alle, Q. *et al.* A single short reprogramming early in life initiates and propagates an epigenetically related mechanism improving fitness and promoting an increased healthy lifespan. *Aging Cell* **21**, e13714 (2022).

26. Sarkar, T. J. *et al.* Transient non-integrative expression of nuclear reprogramming factors promotes multifaceted amelioration of aging in human cells. *Nat. Commun.* **11**, 1545 (2020).
27. de Lázaro, I. *et al.* Non-viral, Tumor-free Induction of Transient Cell Reprogramming in Mouse Skeletal Muscle to Enhance Tissue Regeneration. *Mol. Ther.* **27**, 59–75 (2019).
28. Wang, C. *et al.* In vivo partial reprogramming of myofibers promotes muscle regeneration by remodeling the stem cell niche. *Nat. Commun.* **12**, 3094 (2021).
29. Browder, K. C. *et al.* In vivo partial reprogramming alters age-associated molecular changes during physiological aging in mice. *Nat. Aging* **2**, 243–253 (2022).
30. Chen, Y. *et al.* Reversible reprogramming of cardiomyocytes to a fetal state drives heart regeneration in mice. *Science* **373**, 1537–1540 (2021).
31. Cheng, F. *et al.* Partial reprogramming strategy for intervertebral disc rejuvenation by activating energy switch. *Aging Cell* **21**, e13577 (2022).
32. Lu, Y. *et al.* Reprogramming to recover youthful epigenetic information and restore vision. *Nature* **588**, 124–129 (2020).
33. Gill, D. *et al.* Multi-omic rejuvenation of human cells by maturation phase transient reprogramming. *eLife* **11**, e71624 (2022).
34. Chondronasiou, D. *et al.* Multi-omic rejuvenation of naturally aged tissues by a single cycle of transient reprogramming. *Aging Cell* **21**, e13578 (2022).
35. Maherali, N. *et al.* Directly Reprogrammed Fibroblasts Show Global Epigenetic Remodeling and Widespread Tissue Contribution. *Cell Stem Cell* **1**, 55–70 (2007).
36. Mikkelsen, T. S. *et al.* Dissecting direct reprogramming through integrative genomic analysis. *Nature* **454**, 49–55 (2008).
37. Brambrink, T. *et al.* Sequential Expression of Pluripotency Markers during Direct Reprogramming of Mouse Somatic Cells. *Cell Stem Cell* **2**, 151–159 (2008).
38. Plath, K. & Lowry, W. E. Progress in understanding reprogramming to the induced pluripotent state. *Nat. Rev. Genet.* **12**, 253–265 (2011).
39. Stadtfeld, M., Maherali, N., Breault, D. T. & Hochedlinger, K. Defining Molecular Cornerstones during Fibroblast to iPS Cell Reprogramming in Mouse. *Cell Stem Cell* **2**, 230–240 (2008).

618 40. Li, R. *et al.* A Mesenchymal-to-Epithelial Transition Initiates and Is Required for the Nuclear
619 Reprogramming of Mouse Fibroblasts. *Cell Stem Cell* **7**, 51–63 (2010).
620 41. Samavarchi-Tehrani, P. *et al.* Functional Genomics Reveals a BMP-Driven Mesenchymal-to-
621 Epithelial Transition in the Initiation of Somatic Cell Reprogramming. *Cell Stem Cell* **7**, 64–77
622 (2010).
623 42. Polo, J. M. *et al.* A Molecular Roadmap of Reprogramming Somatic Cells into iPS Cells. *Cell*
624 **151**, 1617–1632 (2012).
625 43. Buganim, Y. *et al.* Single-Cell Expression Analyses during Cellular Reprogramming Reveal
626 an Early Stochastic and a Late Hierarchic Phase. *Cell* **150**, 1209–1222 (2012).
627 44. Benevento, M. *et al.* Proteome adaptation in cell reprogramming proceeds via distinct
628 transcriptional networks. *Nat. Commun.* **5**, 5613 (2014).
629 45. Hansson, J. *et al.* Highly Coordinated Proteome Dynamics during Reprogramming of
630 Somatic Cells to Pluripotency. *Cell Rep.* **2**, 1579–1592 (2012).
631 46. David, L. & Polo, J. M. Phases of reprogramming. *Stem Cell Res.* **12**, 754–761 (2014).
632 47. Kuno, A., Nishimura, K. & Takahashi, S. Time-course transcriptome analysis of human
633 cellular reprogramming from multiple cell types reveals the drastic change occurs between
634 the mid phase and the late phase. *BMC Genomics* **19**, 9 (2018).
635 48. Koche, R. P. *et al.* Reprogramming Factor Expression Initiates Widespread Targeted
636 Chromatin Remodeling. *Cell Stem Cell* **8**, 96–105 (2011).
637 49. Roux, A. E. *et al.* Diverse partial reprogramming strategies restore youthful gene expression
638 and transiently suppress cell identity. *Cell Syst.* **13**, 574-587.e11 (2022).
639 50. Mahmoudi, S. *et al.* Heterogeneity in old fibroblasts is linked to variability in reprogramming
640 and wound healing. *Nature* **574**, 553–558 (2019).
641 51. Ebrahimi, B. Reprogramming barriers and enhancers: strategies to enhance the efficiency
642 and kinetics of induced pluripotency. *Cell Regen.* **4**, 10 (2015).
643 52. Stadtfeld, M. & Hochedlinger, K. Induced pluripotency: history, mechanisms, and
644 applications. *Genes Dev.* **24**, 2239–2263 (2010).
645 53. Bar-Nur, O. *et al.* Small molecules facilitate rapid and synchronous iPSC generation. *Nat.*
646 *Methods* **11**, 1170–1176 (2014).

54. Vidal, S. E., Amlani, B., Chen, T., Tsirigos, A. & Stadtfeld, M. Combinatorial Modulation of Signaling Pathways Reveals Cell-Type-Specific Requirements for Highly Efficient and Synchronous iPSC Reprogramming. *Stem Cell Rep.* **3**, 574–584 (2014).

55. Chen, J. *et al.* Rational optimization of reprogramming culture conditions for the generation of induced pluripotent stem cells with ultra-high efficiency and fast kinetics. *Cell Res.* **21**, 884–894 (2011).

56. Li, W. *et al.* Generation of Human-Induced Pluripotent Stem Cells in the Absence of Exogenous Sox2. *Stem Cells* **27**, 2992–3000 (2009).

57. Liu, X. *et al.* Ascorbic Acid in Epigenetic Reprogramming. *Curr. Stem Cell Res. Ther.* **17**, 13–25 (2022).

58. Esteban, M. A. *et al.* Vitamin C Enhances the Generation of Mouse and Human Induced Pluripotent Stem Cells. *Cell Stem Cell* **6**, 71–79 (2010).

59. Perez, K. *et al.* ERCC1 mice, unlike other premature aging models, display accelerated epigenetic age. 2022.12.28.522011 Preprint at https://doi.org/10.1101/2022.12.28.522011 (2022).

60. Horvath, S. DNA methylation age of human tissues and cell types. *Genome Biol.* **14**, 3156 (2013).

61. Olova, N., Simpson, D. J., Marioni, R. E. & Chandra, T. Partial reprogramming induces a steady decline in epigenetic age before loss of somatic identity. *Aging Cell* **18**, e12877 (2019).

62. Takata, H. *et al.* Chromatin Compaction Protects Genomic DNA from Radiation Damage. *PLoS ONE* **8**, e75622 (2013).

63. Lee, J.-H., Kim, E. W., Croteau, D. L. & Bohr, V. A. Heterochromatin: an epigenetic point of view in aging. *Exp. Mol. Med.* **52**, 1466–1474 (2020).

64. Mah, N. *et al.* Molecular Insights into Reprogramming-Initiation Events Mediated by the OSKM Gene Regulatory Network. *PLOS ONE* **6**, e24351 (2011).

65. Liu, Q. *et al.* Loss of TGFβ signaling increases alternative end-joining DNA repair that sensitizes to genotoxic therapies across cancer types. *Sci. Transl. Med.* **13**, eabc4465 (2021).

66. Kim, B.-G., Malek, E., Choi, S. H., Ignatz-Hoover, J. J. & Driscoll, J. J. Novel therapies emerging in oncology to target the TGF-β pathway. *J. Hematol. Oncol.J Hematol Oncol* **14**, 55 (2021).
67. Tominaga, K. & Suzuki, H. I. TGF-β Signaling in Cellular Senescence and Aging-Related Pathology. *Int. J. Mol. Sci.* **20**, 5002 (2019).
68. Lyu, G. *et al.* TGF-β signaling alters H4K20me3 status via miR-29 and contributes to cellular senescence and cardiac aging. *Nat. Commun.* **9**, 2560 (2018).
69. Schoenfeldt, L. *et al.* Chemical reprogramming ameliorates cellular hallmarks of aging and extends lifespan. 2022.08.29.505222 Preprint at https://doi.org/10.1101/2022.08.29.505222 (2022).
70. Weiss, A. & Attisano, L. The TGFbeta Superfamily Signaling Pathway. *WIREs Dev. Biol.* **2**, 47–63 (2013).
71. Hou, P. *et al.* Pluripotent Stem Cells Induced from Mouse Somatic Cells by Small-Molecule Compounds. *Science* **341**, 651–654 (2013).
72. Guan, J. *et al.* Chemical reprogramming of human somatic cells to pluripotent stem cells. *Nature* **605**, 325–331 (2022).
73. Liu, Q., Lopez, K., Murnane, J., Humphrey, T. & Barcellos-Hoff, M. H. Misrepair in Context: TGFβ Regulation of DNA Repair. *Front. Oncol.* **9**, (2019).
74. Pal, D. *et al.* TGF-β reduces DNA ds-break repair mechanisms to heighten genetic diversity and adaptability of CD44+/CD24− cancer cells. *eLife* **6**, e21615 (2017).
75. Zhang, H. *et al.* TGF-β Inhibition Rescues Hematopoietic Stem Cell Defects and Bone Marrow Failure in Fanconi Anemia. *Cell Stem Cell* **18**, 668–681 (2016).
76. Lu, J. Y. *et al.* Comparative transcriptomics reveals circadian and pluripotency networks as two pillars of longevity regulation. *Cell Metab.* **34**, 836-856.e5 (2022).
77. Kanamoto, T., Hellman, U., Heldin, C.-H. & Souchelnytskyi, S. Functional proteomics of transforming growth factor-β1-stimulated Mv1Lu epithelial cells: Rad51 as a target of TGFβ1-dependent regulation of DNA repair. *EMBO J.* **21**, 1219–1230 (2002).
78. Liu, L. *et al.* TGFβ Induces “BRCAness” and Sensitivity to PARP Inhibition in Breast Cancer by Regulating DNA-Repair Genes. *Mol. Cancer Res.* **12**, 1597–1609 (2014).

79. Lee, J.-Y., Kim, D.-K., Ko, J.-J., Kim, K. P. & Park, K.-S. Rad51 Regulates Reprogramming Efficiency through DNA Repair Pathway. *Dev. Reprod.* **20**, 163–169 (2016).
80. Manukyan, M. & Singh, P. B. Epigenome rejuvenation: HP1β mobility as a measure of pluripotent and senescent chromatin ground states. *Sci. Rep.* **4**, 4789 (2014).
81. López-León, M., Outeiro, T. F. & Goya, R. G. Cell reprogramming: Therapeutic potential and the promise of rejuvenation for the aging brain. *Ageing Res. Rev.* **40**, 168–181 (2017).
82. Carey, B. W., Markoulaki, S., Beard, C., Hanna, J. & Jaenisch, R. Single-gene transgenic mouse strains for reprogramming adult somatic cells. *Nat. Methods* **7**, 56–59 (2010).
83. Stadtfeld, M., Maherali, N., Borkent, M. & Hochedlinger, K. A reprogrammable mouse strain from gene-targeted embryonic stem cells. *Nat. Methods* **7**, 53–55 (2010).
84. Liao, Y., Smyth, G. K. & Shi, W. The Subread aligner: fast, accurate and scalable read mapping by seed-and-vote. *Nucleic Acids Res.* **41**, e108 (2013).
85. Arneson, A. *et al.* A mammalian methylation array for profiling methylation levels at conserved sequences. *Nat. Commun.* **13**, 783 (2022).
86. Zhou, W., Triche, T. J., Jr, Laird, P. W. & Shen, H. SeSAMe: reducing artifactual detection of DNA methylation by Infinium BeadChips in genomic deletions. *Nucleic Acids Res.* **46**, e123 (2018).
87. Boroni, M. *et al.* Highly accurate skin-specific methylome analysis algorithm as a platform to screen and validate therapeutics for healthy aging. *Clin. Epigenetics* **12**, 105 (2020).

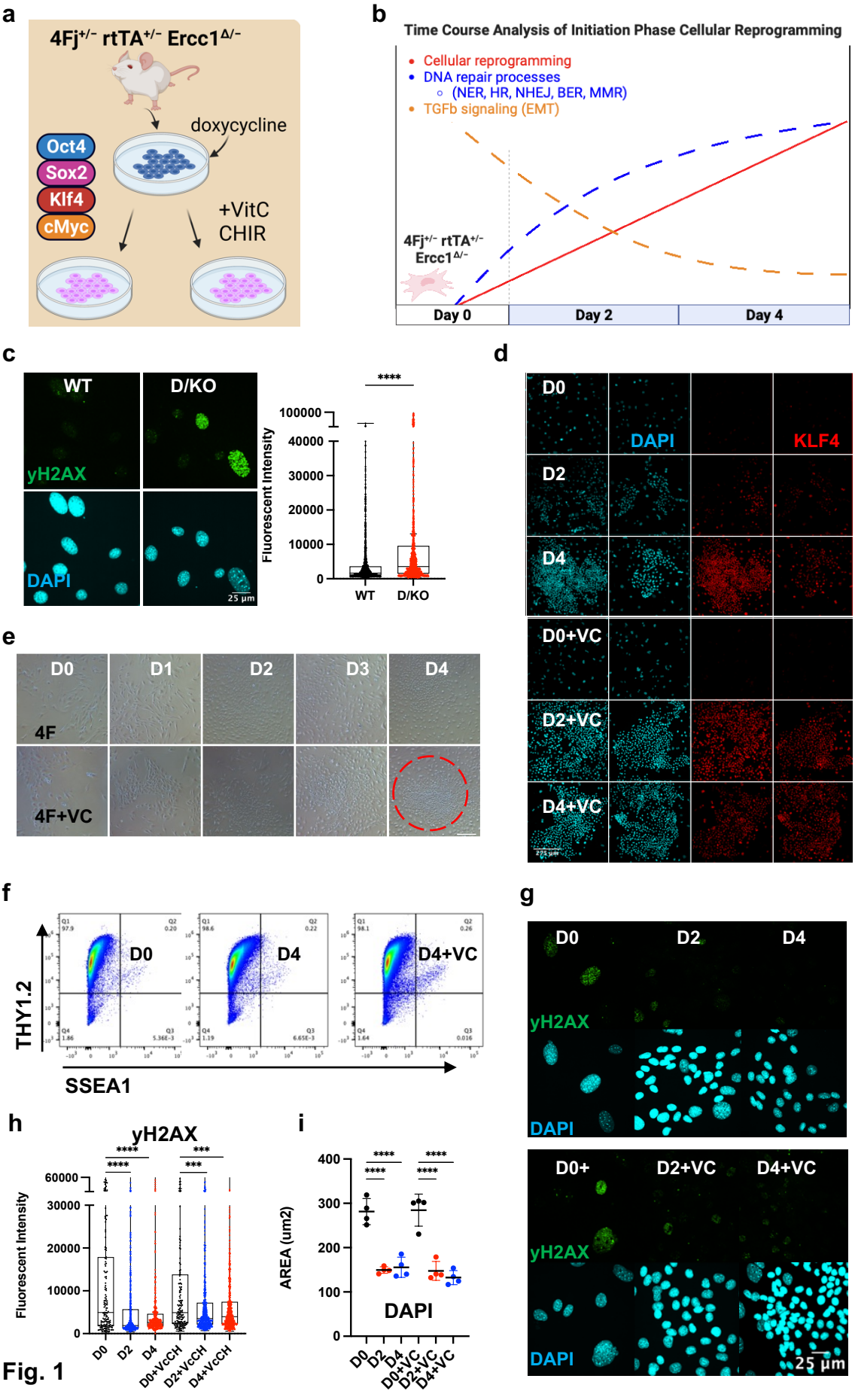
a
4Fj+/- rtTA+/- Ercc1Δ/-
doxycycline
Oct4
Sox2
Klf4
cMyc
+VitC
CHIR
b
Time Course Analysis of Initiation Phase Cellular Reprogramming
Cellular reprogramming
DNA repair processes
(NER, HR, NHEJ, BER, MMR)
TGFb signaling (EMT)
4Fj+/- rtTA+/- Ercc1Δ/-
Day 0
Day 2
Day 4
c
WT
D/KO
yH2AX
DAPI
25 μm
****
Fluorescent Intensity
100000
40000
30000
20000
10000
0
WT
D/KO
d
D0
DAPI
KLF4
D2
D4
D0+VC
D2+VC
D4+VC
e
D0
D1
D2
D3
D4
4F
4F+VC
f
D0
D4
D4+VC
THY1.2
SSEA1
g
D0
D2
D4
yH2AX
DAPI
D0+
D2+VC
D4+VC
yH2AX
DAPI
25 μm
h
yH2AX
Fluorescent Intensity
60000
30000
20000
10000
0
D0
D2
D4
D0+VcCH
D2+VcCH
D4+VcCH
i
AREA (um2)
400
300
200
100
0
DAPI
D0
D2
D4
D0+VC
D2+VC
D4+VC

Fig. 1

Figure 1: Initiation phase reprogramming in 4Fj$^{+/-}$ rtTA$^{+/-}$ Ercc1$^{\Delta/-}$ accelerated aging model promotes DNA damage repair.
(a) Illustration of doxycycline inducible cellular reprogramming Ercc1 mutant fibroblasts (Fb) alone or enhanced with small molecules. **(b)** Schematic of initiation phase timecourse analysis setup with observed changes to DNA repair and TGFb signaling. **(c)** Representative Immunofluorescence (IF) and quantification of yH2AX in fibroblasts from wildtype (WT) and Ercc1$^{\Delta/-}$ (D/KO) mice, imaged with Nikon laser confocal spinning disc, according to Mann-Whitney test, **** p<0.0001. **(d)** IF of KLF4 and DAPI in 4Fj$^{+/-}$ rtTA$^{+/-}$ Ercc1$^{\Delta/-}$ Fbs after 2 and 4 days doxycycline induction with or without VC at 100x **(e)** Time course analysis of 4F and 4F.D/KO Fb during 4 days of dox induction +/- VC, brightfield (BF) images at 4x. **(f)** FACS analysis of reprogramming FBs at day 0 and day 4, stained with Thy1.2 and SSEA1. **(g)** IF of yH2AX and DAPI during time course analysis of 4F.D/KO Fb +/-VC. **(h)** IF quantification of yH2AX levels during timecourse shows decrease levels at day 2 and day 4 according to one way ANOVA, *** p<0.001. **(i)** Quantification of DAPI area during timecourse shows decrease in size at day 2 and day 4 based on mean values of 4 experiments according to one way ANOVA, **** p<0.0001.

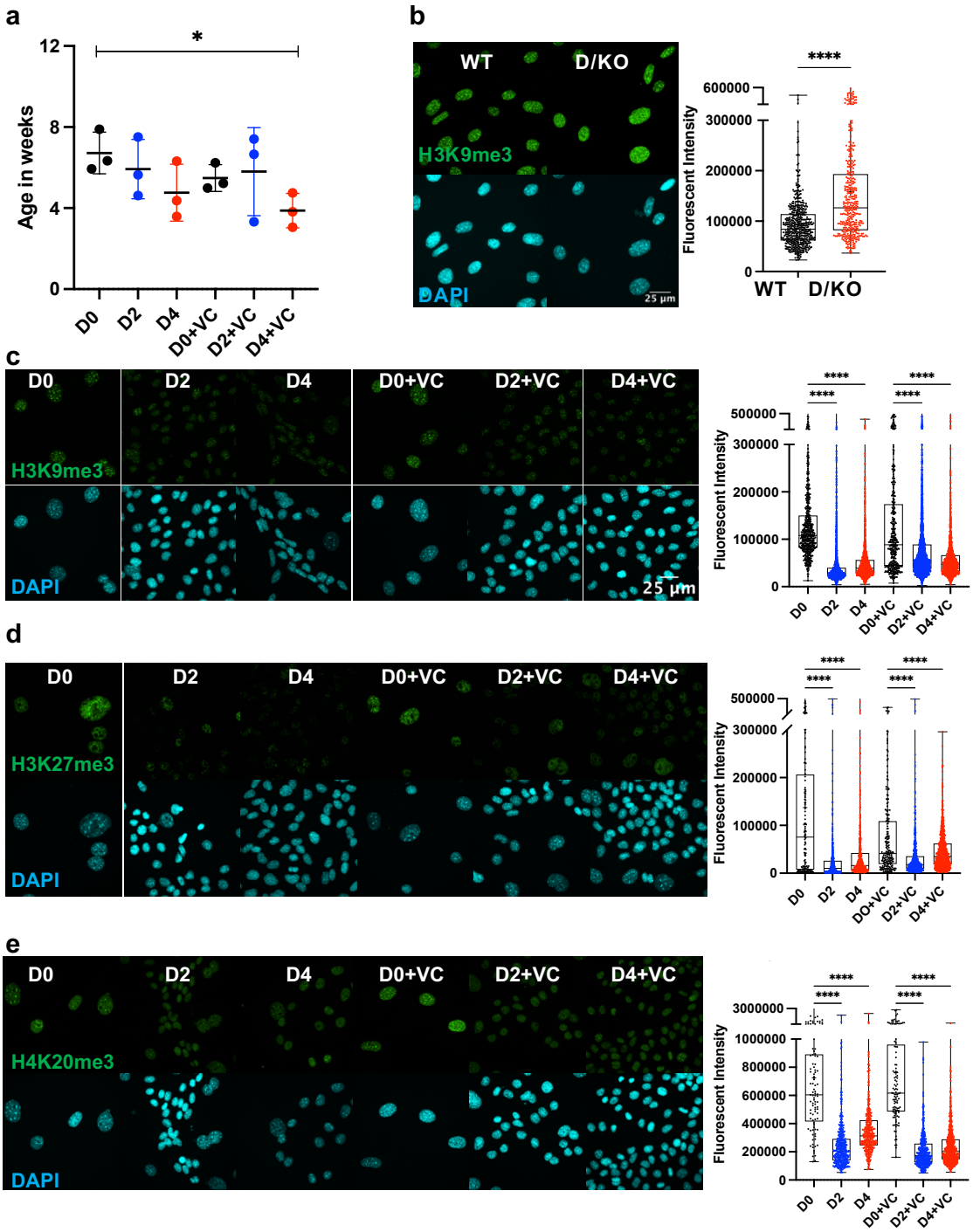
a
Age in weeks
12
8
4
0
*
D0
D2
D4
D0+VC
D2+VC
D4+VC
b
WT
D/KO
H3K9me3
DAPI
25 µm
Fluorescent Intensity
600000
300000
200000
100000
0
****
WT
D/KO
c
H3K9me3
DAPI
25 µm
500000
d
H3K27me3
e
H4K20me3
3000000
1000000
800000
600000
400000

Fig. 2

Figure 2: DNA methylation clock is restored in Ercc1$^{\Delta/-}$ following short term reprogramming.
(a) DNA methylation clock (DNA Methylation Age Skin Final clock) analysis of cellular Ercc1 mutant Fb during time course, n = 3, * $p<0.05$ according to unpaired t-test. **(b)** IF and quantification of H3K9me3 in fibroblasts from WT and D/KO mice, imaged with Nikon laser confocal spinning disc, according to Mann-Whitney test, **** $p<0.0001$. **(c)** IF and quantification of H3K9me3 and DAPI during time course in 4F.D/KO Fbs after 2 and 4 days doxycycline induction with or without VC at 100x according to Kruskal-Wallis test, * $p<0.0001$ **(d)** IF and quantification of H3K27me3 and DAPI during time course in 4F.D/KO Fbs after 2 and 4 days doxycycline induction with or without VC at 100x according to Kruskal-Wallis test, * $p<0.0001$ **(e)** IF and quantification of H4K20me3 and DAPI during time course in 4F.D/KO Fbs after 2 and 4 days doxycycline induction with or without VC at 100x according to Kruskal-Wallis test, * $p<0.0001$.

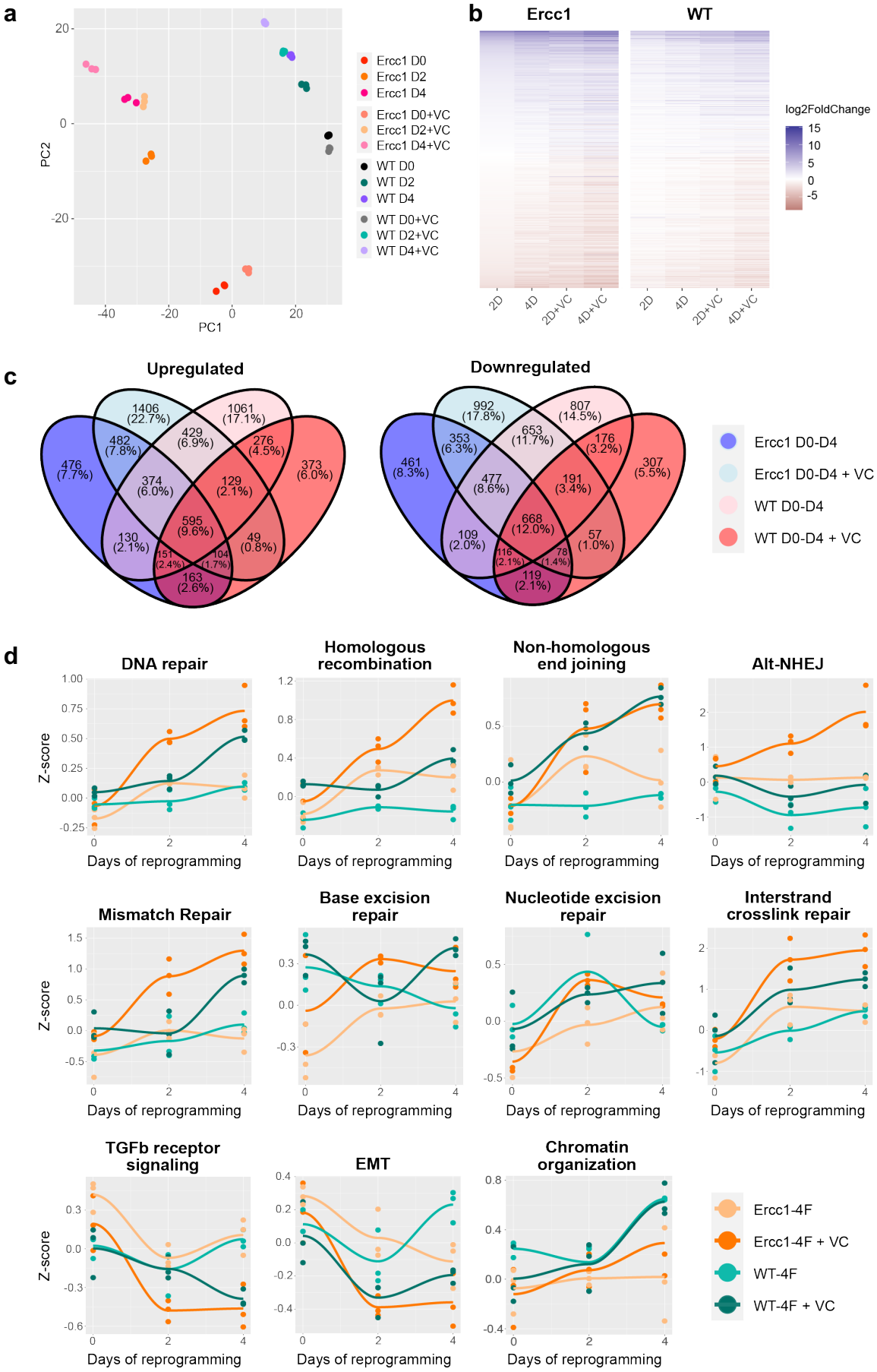
a
PC2
PC1
Ercc1 D0
Ercc1 D2
Ercc1 D4
Ercc1 D0+VC
Ercc1 D2+VC
Ercc1 D4+VC
WT D0
WT D2
WT D4
WT D0+VC
WT D2+VC
WT D4+VC
b
Ercc1
WT
log2FoldChange
2D
4D
2D+VC
4D+VC
c
Upregulated
Downregulated
Ercc1 D0-D4
Ercc1 D0-D4 + VC
WT D0-D4
WT D0-D4 + VC
d
DNA repair
Homologous recombination
Non-homologous end joining
Alt-NHEJ
Mismatch Repair
Base excision repair
Nucleotide excision repair
Interstrand crosslink repair
TGFb receptor signaling
EMT
Chromatin organization
Z-score
Days of reprogramming
Ercc1-4F
Ercc1-4F + VC
WT-4F
WT-4F + VC

Fig. 3

Figure 3: Initation phase reprogramming drives transcriptomic reset and upregulates DNA repair and chromatin organization in Ercc1$^{\Delta/-}$
(a) Principal component analysis (PCA) of the Ercc1 and WT reprogramming at days 0, 2, and 4 with and without VC enhancement. Principal components 1 and 2 are shown. **(b)** Heat map comparing Ercc1 and WT reprogramming at all timepoints, models, and treatements. Genes with a p-value lower than 1e-18 in at least one condition are shown. **(c)** Venn Diagram showing the overlap of significant DEGs (adjusted p-value < 0.05) in Ercc1 and WT during IP reprogramming with and without VC enhancement. Genes were evaluated using a continuous model over 4 days of reprogramming. **(d)** Reprogramming trajectory visualizations based on median Z-scores of genes from significantly up or down regulated GO pathway including DNA repair, TGFb signaling, EMT, and chromatin organization (n=3).

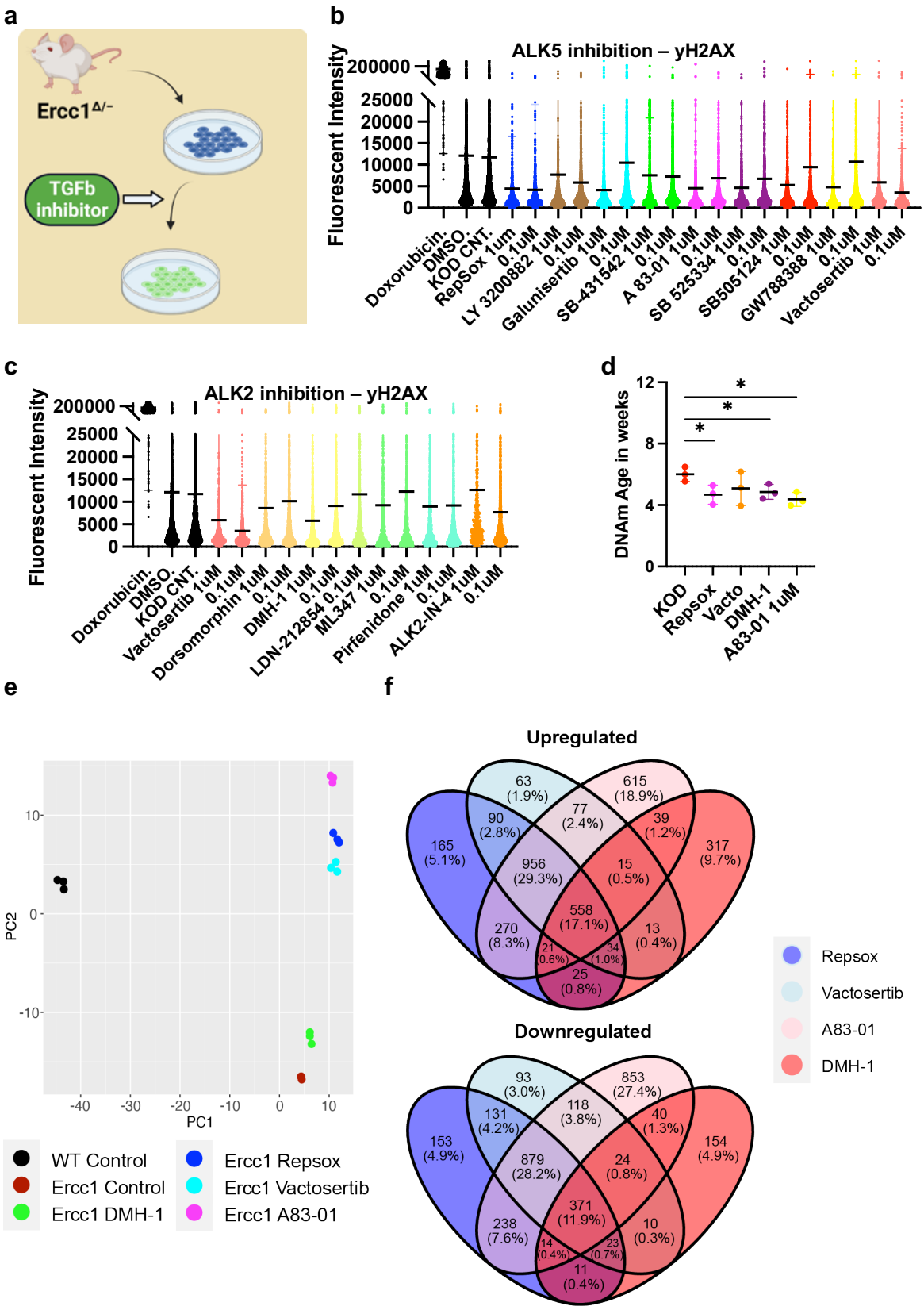
a
Ercc1Δ/-
TGFb inhibitor
b
ALK5 inhibition – yH2AX
Fluorescent Intensity
200000
25000
20000
15000
10000
5000
0
Doxorubicin.
DMSO.
KOD CNT.
RepSox 1um
0.1uM
LY 3200882 1uM
Galunisertib 1uM
SB-431542 1uM
A 83-01 1uM
SB 525334 1uM
SB505124 1uM
GW788388 1uM
Vactosertib 1uM
c
ALK2 inhibition – yH2AX
Fluorescent Intensity
Vactosertib 1uM
Dorsomorphin 1uM
DMH-1 1uM
LDN-212854 0.1uM
ML347 1uM
Pirfenidone 1uM
ALK2-IN-4 1uM
d
DNAm Age in weeks
12
8
4
0
KOD
Repsox
Vacto
DMH-1
A83-01 1uM
e
PC2
PC1
WT Control
Ercc1 Control
Ercc1 DMH-1
Ercc1 Repsox
Ercc1 Vactosertib
Ercc1 A83-01
f
Upregulated
63 (1.9%)
615 (18.9%)
90 (2.8%)
77 (2.4%)
39 (1.2%)
165 (5.1%)
317 (9.7%)
956 (29.3%)
15 (0.5%)
558 (17.1%)
270 (8.3%)
13 (0.4%)
21 (0.6%)
34 (1.0%)
25 (0.8%)
Downregulated
93 (3.0%)
853 (27.4%)
131 (4.2%)
118 (3.8%)
40 (1.3%)
153 (4.9%)
154 (4.9%)
879 (28.2%)
24 (0.8%)
371 (11.9%)
238 (7.6%)
10 (0.3%)
14 (0.4%)
23 (0.7%)
11 (0.4%)
Repsox
Vactosertib
A83-01
DMH-1

Fig. 4

Figure 4: Inhibition of ALK5 or ALK2 receptors improves DNA damage phenotype and resets the DNA methylation clock and transcriptome in Ercc1$^{\Delta/-}$ **(a)** Illustration of TGFb inhibitor screen on D/KO Fbs. **(b)** IF quantification of yH2AX mean levels in D/KO Fbs following treatment with ALK5 inhibitors, plated in 96 wells in triplicate and imaged with laser confocal at 40x. **(c)** IF quantification of yH2AX mean levels in D/KO Fbs following treatment with ALK 2 inhibitors, plated in 96 wells in triplicate. **(d)** DNA methylation clock (DNA Methylation Age Skin Final clock) analysis, comparing Repsox (0.1 um), Vactosertib (0.1 um), DMH-1 (1.0 um), and A83-01 (1.0 um) on D/KO Fbs, n = 3, * $p<0.05$ according to unpaired t-test. **(e)** Principal component analysis (PCA) of Ercc1 cells treated with TGFb inhibitors. Principal components 1 and 2 are shown. **(f)** Venn Diagram showing the overlap of significant genes (adjusted p-value < 0.05) for the TGFb inhibitors.

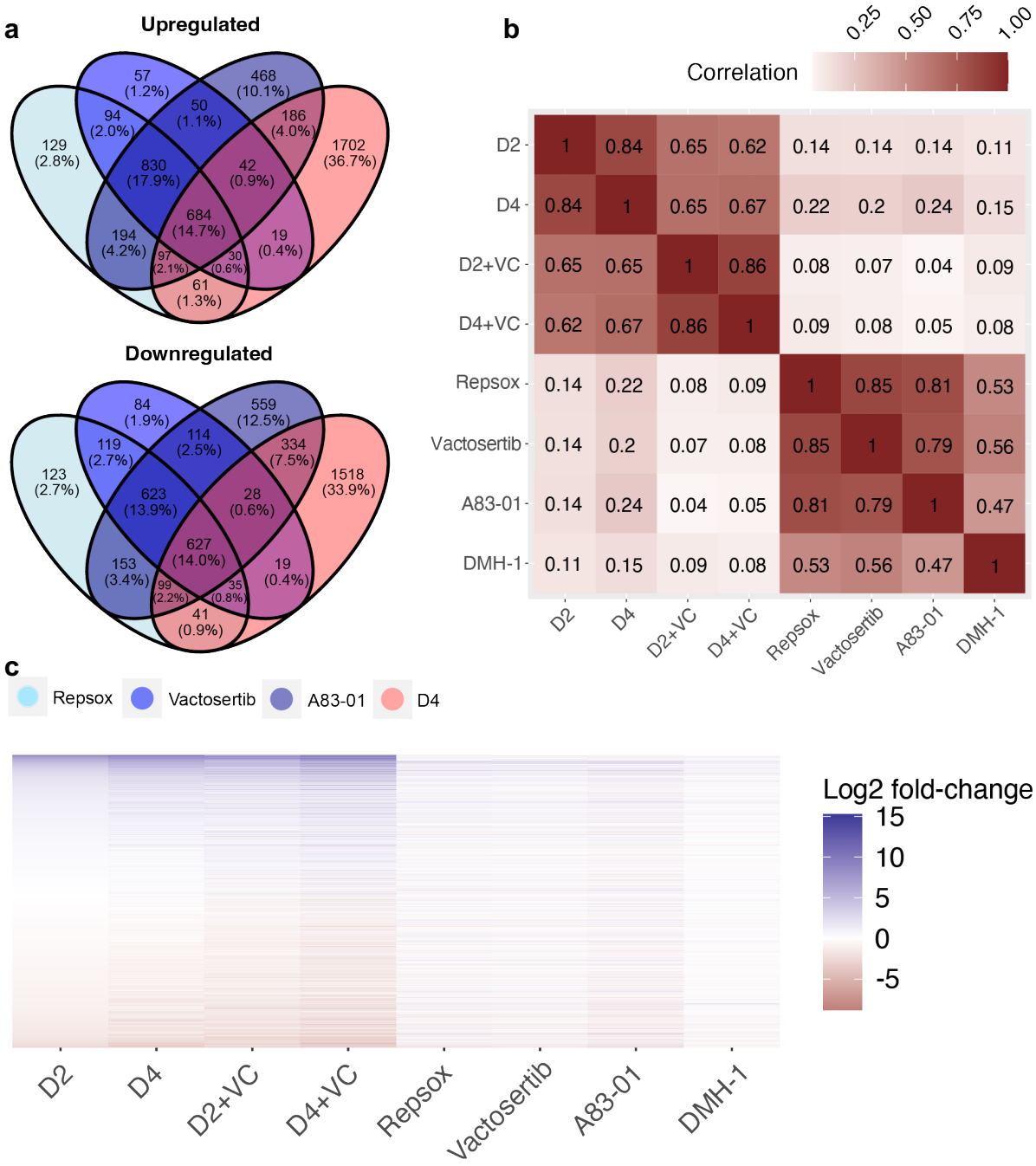
a
Upregulated
57 (1.2%)
468 (10.1%)
50 (1.1%)
94 (2.0%)
186 (4.0%)
129 (2.8%)
1702 (36.7%)
830 (17.9%)
42 (0.9%)
684 (14.7%)
194 (4.2%)
19 (0.4%)
97 (2.1%)
30 (0.6%)
61 (1.3%)
Downregulated
84 (1.9%)
559 (12.5%)
114 (2.5%)
119 (2.7%)
334 (7.5%)
123 (2.7%)
1518 (33.9%)
623 (13.9%)
28 (0.6%)
627 (14.0%)
153 (3.4%)
19 (0.4%)
99 (2.2%)
35 (0.8%)
41 (0.9%)
b
Correlation
0.25
0.50
0.75
1.00
D2 1 0.84 0.65 0.62 0.14 0.14 0.14 0.11
D4 0.84 1 0.65 0.67 0.22 0.2 0.24 0.15
D2+VC 0.65 0.65 1 0.86 0.08 0.07 0.04 0.09
D4+VC 0.62 0.67 0.86 1 0.09 0.08 0.05 0.08
Repsox 0.14 0.22 0.08 0.09 1 0.85 0.81 0.53
Vactosertib 0.14 0.2 0.07 0.08 0.85 1 0.79 0.56
A83-01 0.14 0.24 0.04 0.05 0.81 0.79 1 0.47
DMH-1 0.11 0.15 0.09 0.08 0.53 0.56 0.47 1
D2
D4
D2+VC
D4+VC
Repsox
Vactosertib
A83-01
DMH-1
c
Repsox
Vactosertib
A83-01
D4
Log2 fold-change
15
10
5
0
-5
D2
D4
D2+VC
D4+VC
Repsox
Vactosertib
A83-01
DMH-1
d
Upregulated
Downregulated
GO
ossification
glial cell differentiation
organic hydroxy compound metabolic process
alcohol metabolic process
steroid metabolic process
steroid biosynthetic process
angiogenesis
protein hydroxylation
collagen fibril organization
extracellular structure organization
extracellular matrix organization
external encapsulating structure organization
0
5
10
log(padj)
e
Reactome
Complement cascade
Regulation of Complement cascade
Biological oxidations
Phase I-Functionalization of compounds
Elastic fibre formation
Crosslinking of collagen fibrils
Collagen biosynthesis and modifying enzymes
Assembly of collagen fibrils/multimeric structures
Collagen formation
Extracellular matrix organization
0
5
10
15
log(padj)

Fig. 5

Figure 5: Transcriptomic comparison of Initation phase reprogramming with TGFb inhibition in Ercc1$^{\Delta/-}$. (a) Venn Diagram showing the overlap of significant genes (adjusted p-value < 0.05) for ALK5 inhibitors and 4 days of reprogramming. **(b)** Pairwise correlation between the log2 fold-changes of the filtered gene set (n=16883) of Ercc1 reprogramming and ALK5 or ALK2 inhibitors. **(c)** Heat map comparing Ercc1 reprogramming with TGFb inhibitors. Genes with a p-value lower than 1e-10 in at least one condition are shown. **(d and e)** GO and Reactome analysis of the intersect of significant genes as evaluated in 5A. Terms with the top six upregulated (red) and downregulated (blue) assessed by log(adjusted p-value) are shown.

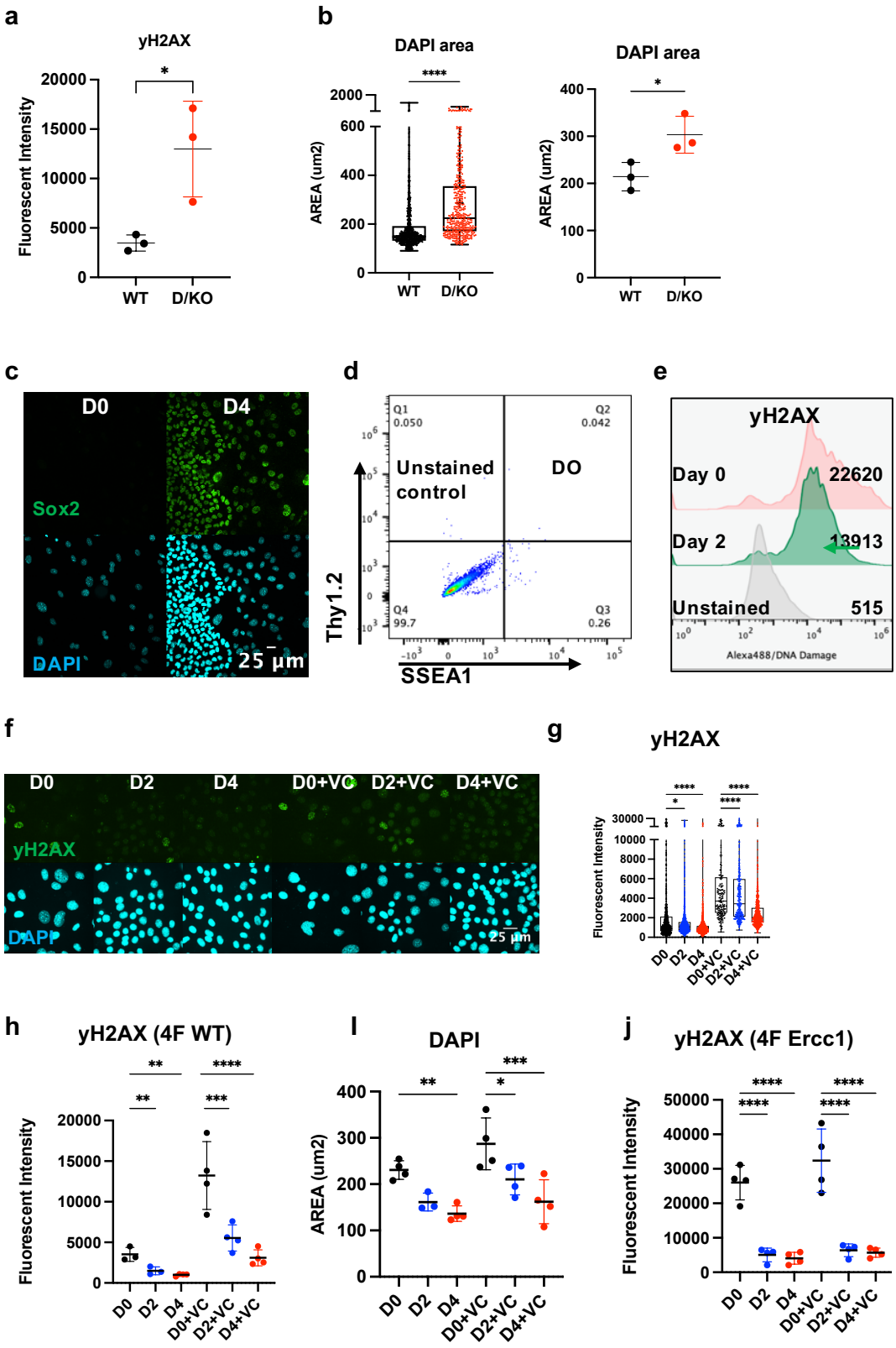
a
yH2AX
Fluorescent Intensity
20000
15000
10000
5000
0
*
WT
D/KO
b
DAPI area
AREA (um2)
2000
600
400
200
0
****
WT
D/KO
DAPI area
AREA (um2)
400
300
200
100
0
*
WT
D/KO
c
D0
D4
Sox2
DAPI
25 µm
d
Q1
0.050
Q2
0.042
Unstained
control
DO
Q4
99.7
Q3
0.26
Thy1.2
SSEA1
e
yH2AX
Day 0
22620
Day 2
13913
Unstained
515
Alexa488/DNA Damage
f
D0
D2
D4
D0+VC
D2+VC
D4+VC
yH2AX
DAPI
25 µm
g
yH2AX
Fluorescent Intensity
30000
10000
8000
6000
4000
2000
0
****
*
****
****
D0
D2
D4
D0+VC
D2+VC
D4+VC
h
yH2AX (4F WT)
Fluorescent Intensity
20000
15000
10000
5000
0
**
**
****
***
D0
D2
D4
D0+VC
D2+VC
D4+VC
I
DAPI
AREA (um2)
400
300
200
100
0
**
***
*
D0
D2
D4
D0+VC
D2+VC
D4+VC
j
yH2AX (4F Ercc1)
Fluorescent Intensity
50000
40000
30000
20000
10000
0
****
****
****
****
D0
D2
D4
D0+VC
D2+VC
D4+VC

Fig. S1

Figure S1: Initiation phase reprogramming in 4Fj$^{+/-}$ rtTA$^{+/-}$ Ercc1$^{\Delta/-}$ accelerated aging model promotes DNA damage repair.
(a) Quantification of yH2AX IF from 3 experiments in fibroblasts from wildtype (WT) and Ercc1$^{\Delta/-}$ (D/KO) mice, imaged with Nikon laser confocal spinning disc, according to unpaired t-test, * p<0.05. **(b)**. Quantification of DAPI in fibroblasts from wildtype (WT) and Ercc1$^{\Delta/-}$ (D/KO) mice, imaged with Nikon laser confocal spinning disc, according to Mann-Whitney test, **** p<0.0001. Quantification of DAPI area from 3 experiments in fibroblasts from wildtype (WT) and Ercc1$^{\Delta/-}$ (D/KO) mice, imaged with Nikon laser confocal spinning disc, according to unpaired t-test, * p<0.05 **(c)** IF image of Sox2 and DAPI in 4F.D/KO Fbs after 4 days doxycycline induction, 40x **(d)** FACS unstained control for analysis of reprogramming Fbs markers Thy1.2 and SSEA1. **(e)** FACS analysis yH2AX levels following reprogramming of 4F.D/KO Fbs at day 0, day 2, and unstained control. **(f)** IF images of yH2AX and DAPI during representative time course analysis of 4F.WT Fb +/-VC at 100x. **(g)** Quantification of yH2AX images during time course shows significantly decreased levels at day 2 and day 4 according to one way ANOVA, **** p<0.0001. **(h)** Quantification of mean yH2AX levels in 4F WT from 3 or 4 experiments during time course shows significant decrease to levels at day 2 and day 4 according to one way ANOVA, ** p<0.01. **(i)** Quantification of DAPI area during time course shows decrease in size at day 2 and day 4 based on mean values of 4 experiments according to one way ANOVA, *** p<0.001, ** p<0.01, *p<0.05. **(j)** Quantification of mean yH2AX levels in 4F D/KO from 4 experiments during time course shows significant decrease to levels at day 2 and day 4 according to one way ANOVA, ** p<0.0001.

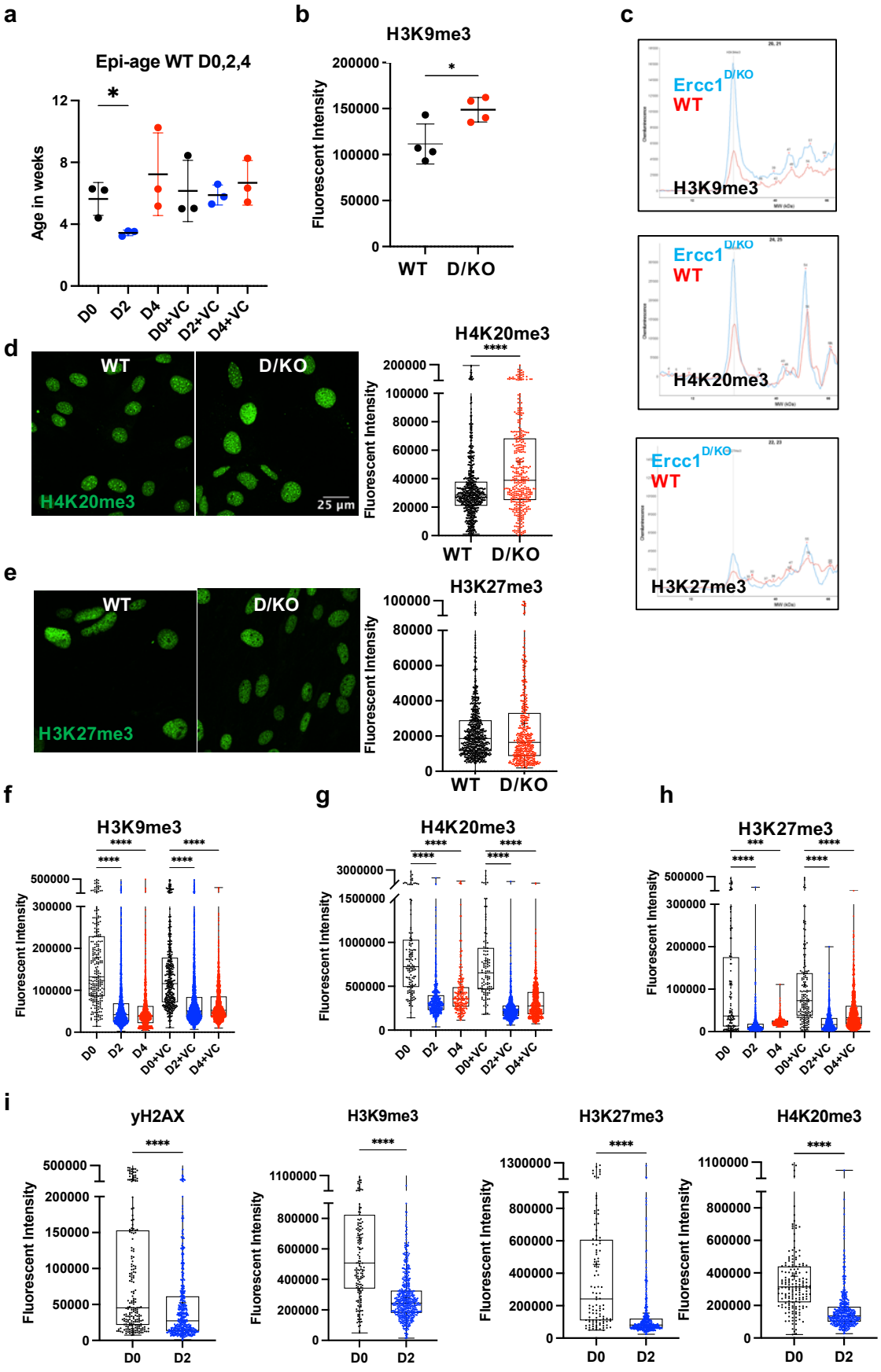
a
Epi-age WT D0,2,4
Age in weeks
D0
D2
D4
D0+VC
D2+VC
D4+VC
b
H3K9me3
Fluorescent Intensity
WT
D/KO
c
Ercc1 D/KO
WT
H3K9me3
H4K20me3
H3K27me3
d
WT
D/KO
H4K20me3
25 µm
e
H3K27me3
f
H3K9me3
g
H4K20me3
h
H3K27me3
i
yH2AX
H3K9me3
H3K27me3
H4K20me3

Fig. S2

Figure S2: DNA methylation clock is restored in Ercc1$^{\Delta/-}$ following short term reprogramming.
(a) DNA Methylation Age Skin Final clock analysis of WT Fb during time course, n = 3, * $p<0.05$ according to unpaired t-test. **(b)** Quantification of mean values of H3K9me3 levels in fibroblasts from WT and D/KO mice (n=4) according to unpaired t-test, * $p<0.05$. (**c)** Western capillary chemiluminescence quantification shows increased H3K9me3 and H4K20me3, with unchanged H3K27me3 in fibroblasts from D/KO vs WT mice (n=1 each). **(d)** IF and quantification shows increased H4K20me3 in fibroblasts from D/KO mice vs WT, imaged with Nikon laser confocal spinning disc, according to Mann-Whitney test, **** $p<0.0001$ **(e)** IF quantification shows unchaged H3K27me3 in fibroblasts from WT and D/KO mice, imaged with Nikon laser confocal spinning disc. **(f, g,h)** IF quantification of 2nd experiment shows significantly decreased H3K9me3, H4K20me3, and H3K27me3 levels during time course in 4F.D/KO Fbs after 2 and 4 days doxycycline induction with or without VC at 100x according to Kruskal-Wallis test, * $p<0.000$. **(i)** IF quantification of 3rd experiment shows yH2AX, H3K9me3, H4K20me3, and H3K27me3 in 4F.D/KO Fbs after 2 doxycycline induction at 100x according to Mann-Whitney test, * $p<0.000$.

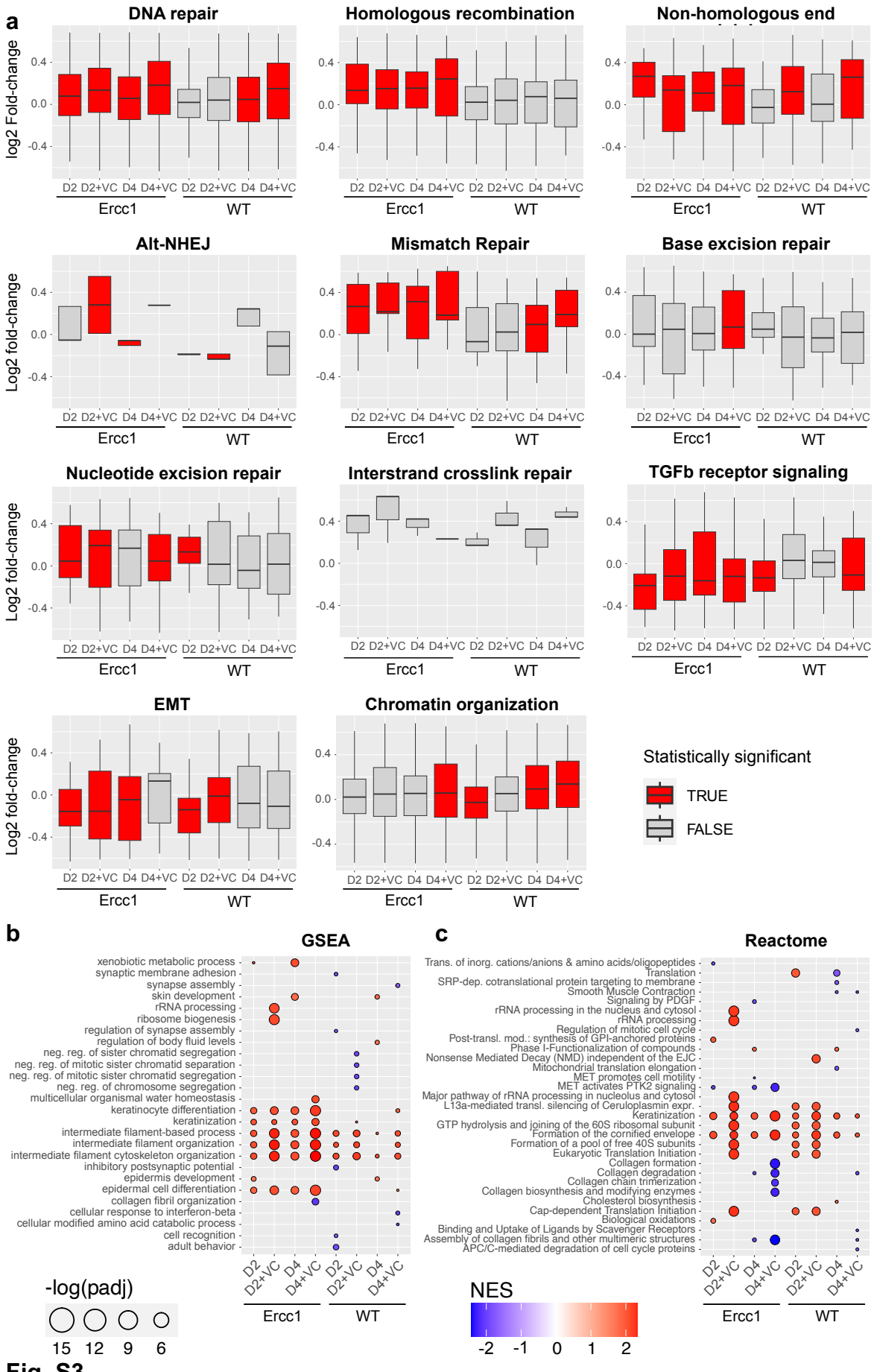
a
DNA repair
Homologous recombination
Non-homologous end
Alt-NHEJ
Mismatch Repair
Base excision repair
Nucleotide excision repair
Interstrand crosslink repair
TGFb receptor signaling
EMT
Chromatin organization
log2 Fold-change
Log2 fold-change
0.4
0.0
-0.4
D2 D2+VC D4 D4+VC D2 D2+VC D4 D4+VC
Ercc1
WT
Statistically significant
TRUE
FALSE
b
GSEA
xenobiotic metabolic process
synaptic membrane adhesion
synapse assembly
skin development
rRNA processing
ribosome biogenesis
regulation of synapse assembly
regulation of body fluid levels
neg. reg. of sister chromatid segregation
neg. reg. of mitotic sister chromatid separation
neg. reg. of mitotic sister chromatid segregation
neg. reg. of chromosome segregation
multicellular organismal water homeostasis
keratinocyte differentiation
keratinization
intermediate filament-based process
intermediate filament organization
intermediate filament cytoskeleton organization
inhibitory postsynaptic potential
epidermis development
epidermal cell differentiation
collagen fibril organization
cellular response to interferon-beta
cellular modified amino acid catabolic process
cell recognition
adult behavior
D2 D2+VC D4 D4+VC D2 D2+VC D4 D4+VC
Ercc1
WT
-log(padj)
15 12 9 6
c
Reactome
Trans. of inorg. cations/anions & amino acids/oligopeptides
Translation
SRP-dep. cotranslational protein targeting to membrane
Smooth Muscle Contraction
Signaling by PDGF
rRNA processing in the nucleus and cytosol
rRNA processing
Regulation of mitotic cell cycle
Post-transl. mod.: synthesis of GPI-anchored proteins
Phase I-Functionalization of compounds
Nonsense Mediated Decay (NMD) independent of the EJC
Mitochondrial translation elongation
MET promotes cell motility
MET activates PTK2 signaling
Major pathway of rRNA processing in nucleolus and cytosol
L13a-mediated transl. silencing of Ceruloplasmin expr.
Keratinization
GTP hydrolysis and joining of the 60S ribosomal subunit
Formation of the cornified envelope
Formation of a pool of free 40S subunits
Eukaryotic Translation Initiation
Collagen formation
Collagen degradation
Collagen chain trimerization
Collagen biosynthesis and modifying enzymes
Cholesterol biosynthesis
Cap-dependent Translation Initiation
Biological oxidations
Binding and Uptake of Ligands by Scavenger Receptors
Assembly of collagen fibrils and other multimeric structures
APC/C-mediated degradation of cell cycle proteins
D2 D2+VC D4 D4+VC D2 D2+VC D4 D4+VC
Ercc1
WT
NES
-2 -1 0 1 2

Fig. S3

Figure S3: Initation phase reprogramming drives transcriptomic reset and upregulates DNA repair and chromatin organization in Ercc1$^{\Delta/-}$
(a) Log2 fold-change of genes within a given GO pathway for Ercc1 and WT reprogramming at days 0, 2, and 4 with and without VC enhancement. The inner boxplot depicts medians and the first and third quartiles, with whiskers extending up to the 1.5x interquartile range and outliers removed for improved visualization of differences between conditions. Statistical significance (Wilcoxon Test, p-value < 0.05) is indicated by red coloring. **(b and c)** GSEA and Reactome analysis of Ercc1 and WT reprogramming considering log2 fold-changes between day 0 and day 2 of reprogramming and day 0 and day 4 of reprogramming with and without VC enhancement. Gene ontology biological process terms and Reactome terms are plotted against the normalized enrichment score (NES) with -log(adjusted p-value) illustrated through circle size. The top 10 terms for each condition are included.

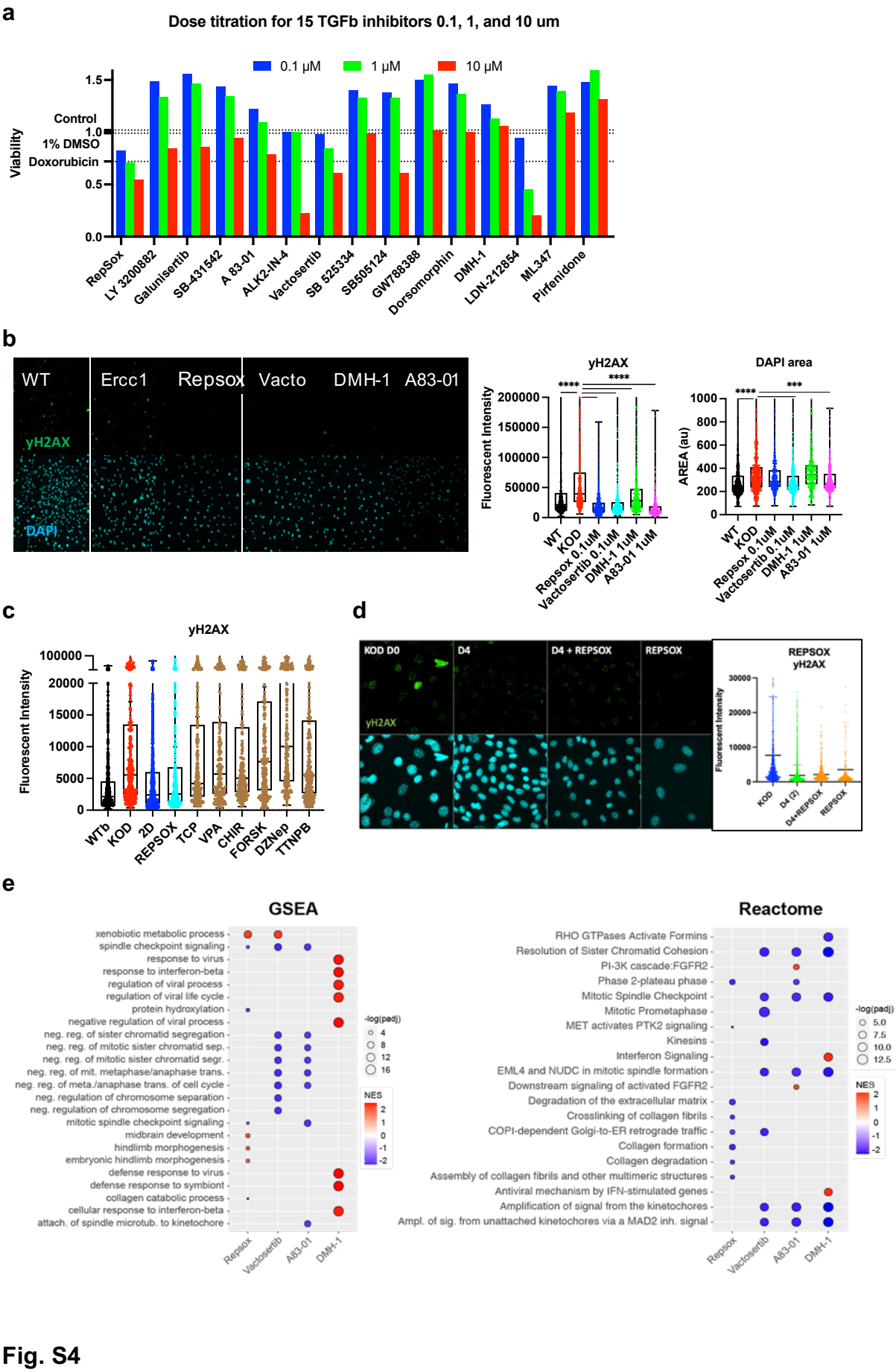
a
Dose titration for 15 TGFb inhibitors 0.1, 1, and 10 um
0.1 µM
1 µM
10 µM
Viability
Control
1% DMSO
Doxorubicin
RepSox
LY 3200882
Galunisertib
SB-431542
A 83-01
ALK2-IN-4
Vactosertib
SB 525334
SB505124
GW788388
Dorsomorphin
DMH-1
LDN-212854
ML347
Pirfenidone
b
WT
Ercc1
Repsox
Vacto
DMH-1
A83-01
yH2AX
DAPI
yH2AX
Fluorescent Intensity
DAPI area
AREA (au)
WT
KOD
Repsox 0.1uM
Vactosertib 0.1uM
DMH-1 1uM
A83-01 1uM
c
yH2AX
Fluorescent Intensity
WTb
KOD
2D
REPSOX
TCP
VPA
CHIR
FORSK
DZNep
TTNPB
d
KOD D0
D4
D4 + REPSOX
REPSOX
yH2AX
REPSOX
yH2AX
Fluorescent Intensity
KOD
D4 (2)
D4+REPSOX
REPSOX
e
GSEA
xenobiotic metabolic process
spindle checkpoint signaling
response to virus
response to interferon-beta
regulation of viral process
regulation of viral life cycle
protein hydroxylation
negative regulation of viral process
neg. reg. of sister chromatid segregation
neg. reg. of mitotic sister chromatid sep.
neg. reg. of mitotic sister chromatid segr.
neg. reg. of mit. metaphase/anaphase trans.
neg. reg. of meta./anaphase trans. of cell cycle
neg. regulation of chromosome separation
neg. regulation of chromosome segregation
mitotic spindle checkpoint signaling
midbrain development
hindlimb morphogenesis
embryonic hindlimb morphogenesis
defense response to virus
defense response to symbiont
collagen catabolic process
cellular response to interferon-beta
attach. of spindle microtub. to kinetochore
-log(padj)
NES
Repsox
Vactosertib
A83-01
DMH-1
Reactome
RHO GTPases Activate Formins
Resolution of Sister Chromatid Cohesion
PI-3K cascade:FGFR2
Phase 2-plateau phase
Mitotic Spindle Checkpoint
Mitotic Prometaphase
MET activates PTK2 signaling
Kinesins
Interferon Signaling
EML4 and NUDC in mitotic spindle formation
Downstream signaling of activated FGFR2
Degradation of the extracellular matrix
Crosslinking of collagen fibrils
COPI-dependent Golgi-to-ER retrograde traffic
Collagen formation
Collagen degradation
Assembly of collagen fibrils and other multimeric structures
Antiviral mechanism by IFN-stimulated genes
Amplification of signal from the kinetochores
Ampl. of sig. from unattached kinetochores via a MAD2 inh. signal
-log(padj)
NES
Repsox
Vactosertib
A83-01
DMH-1

Fig. S4

Figure S4: Inhibition of ALK5 or ALK2 receptors improves DNA damage phenotype and resets the DNA methylation clock and transcriptome in Ercc1$^{\Delta/-}$ **(a)** Cell viability quantification using MTS assay in 96 well plates following treatment with high, medium, and low concentrations of 15 inhibitors in triplicate. Dosage range is 10um, 1um, and 0.1 um. Controls are represented by dashed lines and include untreated D/KO Fbs, 1% DMSO, and Doxorubicin (0.1um). **(b)** IF images and quantification of yH2AX levels and DAPI area in WT vs D/KO Fbs treated with Repsox, Vactosertib, DMH-1, and A83-01 in 24 wells plates, n = 1. **(c)** IF quantification of yH2AX levels comparing 2 days of doxycline induction to seven single small molecules used in chemical reprogramming at published dosages: Repsox (3um), TCP (10um), VPA (500um), CHIR99021 (5um), Forskolin (10um), DZNep (0.5um), and TTNPB (1um), n = 1. **(d)** IF images and quantification of yH2AX levels in 4F.D/KO cells after 4 days of induction either with doxycycline alone, doxycycline and Repsox, or Repsox alone, n = 1. **(e)** GSEA and Reactome analysis of Ercc1 cells treated with TGFb inhibitors considering log2 fold-changes, n = 3. Gene ontology biological process terms or Reactome terms are plotted against the normalized enrichment score (NES) with -log(adjusted p-value) indicated through circle size. The top 10 terms for each condition are included.

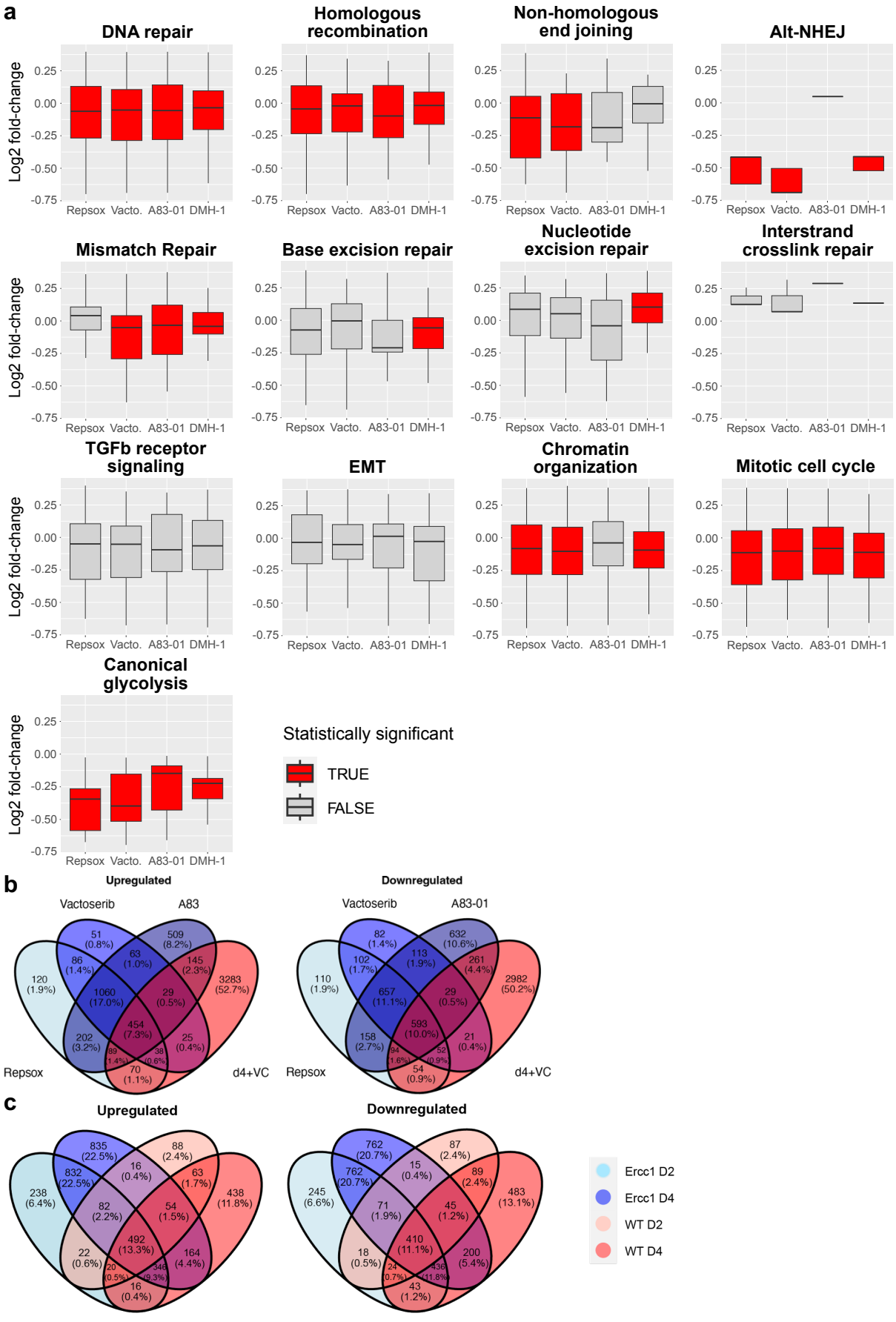
a
DNA repair
Homologous recombination
Non-homologous end joining
Alt-NHEJ
Mismatch Repair
Base excision repair
Nucleotide excision repair
Interstrand crosslink repair
TGFb receptor signaling
EMT
Chromatin organization
Mitotic cell cycle
Canonical glycolysis
Log2 fold-change
0.25
0.00
-0.25
-0.50
-0.75
Repsox
Vacto.
A83-01
DMH-1
Statistically significant
TRUE
FALSE
b
Upregulated
Vactoserib
A83
120 (1.9%)
51 (0.8%)
509 (8.2%)
86 (1.4%)
63 (1.0%)
145 (2.3%)
3283 (52.7%)
1060 (17.0%)
29 (0.5%)
454 (7.3%)
202 (3.2%)
89 (1.4%)
38 (0.6%)
25 (0.4%)
70 (1.1%)
Repsox
d4+VC
Downregulated
Vactoserib
A83-01
110 (1.9%)
82 (1.4%)
632 (10.6%)
102 (1.7%)
113 (1.9%)
261 (4.4%)
2982 (50.2%)
657 (11.1%)
29 (0.5%)
593 (10.0%)
158 (2.7%)
94 (1.6%)
52 (0.9%)
21 (0.4%)
54 (0.9%)
Repsox
d4+VC
c
Upregulated
238 (6.4%)
835 (22.5%)
88 (2.4%)
832 (22.5%)
16 (0.4%)
63 (1.7%)
438 (11.8%)
82 (2.2%)
54 (1.5%)
492 (13.3%)
22 (0.6%)
20 (0.5%)
346 (9.3%)
164 (4.4%)
16 (0.4%)
Downregulated
245 (6.6%)
762 (20.7%)
87 (2.4%)
762 (20.7%)
15 (0.4%)
89 (2.4%)
483 (13.1%)
71 (1.9%)
45 (1.2%)
410 (11.1%)
18 (0.5%)
24 (0.7%)
436 (11.8%)
200 (5.4%)
43 (1.2%)
Ercc1 D2
Ercc1 D4
WT D2
WT D4

Fig. S5

Figure S5: GO term analysis of TGFb inhibition in Ercc1$^{\Delta/-}$. (a) Log2 fold-change of genes within a given GO pathway for Ercc1 cells treated with TGFb inhibitors compared to non-treated Ercc1 cells. The inner boxplot depicts medians and the first and third quartiles, with whiskers extending up to the 1.5x interquartile range and outliers removed for improved visualization of differences between conditions. Statistical significance (Wilcoxon Test, p-value < 0.05) is indicated by red coloring. **(b)** Venn Diagram showing the overlap of significant genes (adjusted p-value < 0.05) for the ALK5 inhibitors and enhanced reprogramming day 4+VC. **(c)** Venn Diagram showing the overlap of significant genes (adjusted p-value < 0.05) for the reprogramming time course at day 2 and 4 without VC.